Applied Mathematical Modelling 78 (2020) 968–988

Contents lists available at ScienceDirect

Applied Mathematical Modelling

journal homepage: www.elsevier.com/locate/apm

Relativistic HPIC-LBM and its application in large temporal-spatial turbulent magnetic reconnection. Part II. Role of turbulence in the flux rope interaction

Bojing Zhu[a,b,1,*], Hui Yan[c], Ying Zhong[c], Jingkun Chen[c], Yunfei Du[c], Huihong Cheng[d,e], David A Yuen[f]

[a] Yunnan Observatories, Chinese Academy of Sciences, Kunming 650216, China
[b] Center for Astronomical Mega-Science, Chinese Academy of Sciences, Beijing 100012, China
[c] National Supercomputer Center in Guangzhou, Sun Yat-sen University, Guangzhou 510006, China
[d] Key Laboratory of Computing Geodynamics, Chinese Academy of Sciences, Beijing 100049, China
[e] College of Earth and Planetary Sciences, University of Chinese Academy of Sciences, Beijing 100049, China
[f] Applied Physics and Applied Mathematics Department, Columbia University, New York 10027, USA

A R T I C L E I N F O

Article history:
Received 13 November 2018
Revised 18 February 2019
Accepted 15 May 2019
Available online 24 May 2019

Keywords:
Relativistic HPIC-LBM
3D LTSTMR
Oblique instability
Turbulent acceleration mechanism
Slipping magnetic reconnection (1st type MR)
Magnetic field line break-rejoin magnetic reconnection (2nd type MR)
Magnetic energy conversion

A B S T R A C T

Quantitatively analyzing the role of turbulence in the magnetic fluctuation-induced self-generating-organization region and the plasma turbulence-induced self-feeding-sustaining region, which is closely related to the evolution of null points and the magnetic helical structure, represents the key issues in understanding the magnetic energy release-conversion, plasma heating, and charged particles energization and acceleration in three-dimensional large temporal-spatial scale turbulent magnetic reconnection (3D LTSTMR). The first part of this two-paper series developed and validated the continuous kinetic-dynamic-hydro fully coupled temporal-spatial scale relativistic hybrid particle-in-cell and lattice Boltzmann (RHPIC-LBM) model and code for investigating the fine structure evolution of the 2.5D solar atmosphere LTSTMR activities. Based on the model and code developed in Part I, in this paper, we investigate the turbulence of the magnetic helical structure, current density vector fields, self-generating-organization magnetic potential vector fields, self-feeding-sustaining plasma motion, and the ion and electron acceleration of 3D LTSTMR with 100,000 CPU cores on the ***Tianhe-2*** from National Supercomputer Center in Guang Zhou (NSCC-GZ). According to the simulation evidence, we discovered and confirmed the following results: (i) Slipping magnetic reconnection (MR) exists in the adjacent magnetic field lines (MFLs) during the compress-stretch-slip process on the quasi-separatrix layers (QSLs and MFLs drastically change and form a linkage span) and the adjacent MFLs' break-rejoin MR exists on the separatrix surfaces (SLs). Both are consistent to observations; (ii) The slipping MR (defined as 1st type MR) and the MFLs' break-rejoin MR (defined as 2nd type MR) are closely linked with the oblique and resistive tearing instabilities, respectively. In the 3D model, the 1st type MR forms *O*-type null points, while the 2nd type MR forms *X*-type null points. The magnetic energy conversion is dominated by turbulence-induced oblique instabilities in the 3D model instead of the resistive tearing instabilities in the 2D/2.5D model, which is consistent with the 3D observations;

* Corresponding author at: Yunnan Observatories, Chinese Academy of Sciences, Kunming 650216, China.
E-mail addresses: bjzhu@ynao.ac.cn, cynosureorion@ucas.ac.cn (B. Zhu).

[1] Hui Yan, Jingkun Chen, Ying Zhong and Yunfei Du conceived Tianhe-2 simulation; David A yuen conceived the hurst index research in rhpic-lbm model; huihong cheng conceived the LBM model and verified its application in Geophysics.

https://doi.org/10.1016/j.apm.2019.05.027

(iii) Magnetic energy conversion occurs in the interaction of the plasmoid-to-flux rope, plasmoid-to-plasmoid, and flux rope-to-flux rope. The turbulent acceleration is an independent acceleration mechanism in LTSTMR, induced by the interaction of waves-to-waves and waves-to-particles, which is different from the original hybrid acceleration mechanism (composed of parallel electric fields, betatron, shock and Fermi) ; (iv) Particles can be energized and accelerated at a longer time scale (−30 s) and can be accelerated to relativistic energies after being pre-accelerated by a Fermi-Betatron-shock wave acceleration process. These results are in agreement with the observations.

1. Introduction

Magnetic reconnection (MR) is universally recognized as a key ingredient in the behavior of many laboratory plasma, Earth's plasma, space physical plasma, and astronomical & astrophysical plasmas, including the interiors and atmospheres of stars and planets, such as Earth's ionosphere-magnetospheres, solar atmospheric activities, planetary magnetospheres, accretion disks, and pulsar magnetospheres [1,2].

As seen from Table 1, part of the MR explosive phenomena belongs to large spatial scale and short temporal scale evolutions (black holes, neutron stars, and supernovae), while the other MR explosive phenomena belong to large spatial scale and long temporal scales evolutions (pulsar nebulae flare, solar flare, solar wind).

In our research, we define the latter phenomenon as large temporal-spatial scale turbulent magnetic reconnection (LTSTMR). Observations of the sun show that the solar atmosphere activities are typical continuous kinetic-dynamic-hydro fully coupled LTSTMR (Table 2; e.g., limb, flare and coronal mass ejection [CME]),which includes many kinetic scale fractal magnetic structures (self-similarity characteristic) and turbulence MRs (turbulence filling ability).

Additionally, the solar atmosphere LTSTMR activities cover the picoscale ($10^{-2}\ m \sim 10^{5}\ m$), nanoscale ($10^{5}\ m \sim 10^{6}\ m$), microscale ($10^{6}\ m \sim 10^{7}\ m$), macroscale ($10^{7}\ m \sim 10^{8}\ m$) and large hydroscale ($10^{8}\ m \sim 10^{9}\ m$).

Thus, it is hard to cover all scales of the phenomena from one concept when defining a temporal-spatial scale for this kind of ubiquitous phenomenon.

In this paper, we defined an LTSTMR for Earth's ionosphere-magnetospheres, space physics, and solar atmosphere activities that satisfies all the following conditions:

(i) The spatial scale is defined by using the characteristic length of the electron, which is equal to the electron's *Larmor* radius ($r_e = V_{T_e}/\omega_{ce} = \frac{\kappa^{1/2} T_e^{1/2} m_e^{1/2} c}{eB}$) and the electron's inertial length ($d_e = {}^{c}/_{\omega_{pe}} = \frac{m_e^{1/2}}{2\pi^{1/2} n_e^{1/2} e}$) for the low-$\beta$ case and high-β case, respectively.

(ii) The temporal scale is defined using the electron cyclotron time $\Omega_{ce} = \omega_{ce}^{-1} = q\boldsymbol{B}/m_e c$.

(iii) The observed current sheets' (CS) thickness used to characterize the length of the electron ratio is of the $10^{10} \sim 10^{11}$ order.

(iv) The observed evolution time of the electron cyclotron time ratio is of the $10^{10} \sim 10^{11}$ order.

The mechanism of the magnetic energy release and the process of its transfer to heating and accelerating nonthermal particles in the diffusion region are the key issues in 3D LTSTMR.

While the mechanism of the role of turbulence in these processes is still a matter of considerable debate, recent research from observational evidence and theoretical arguments show that most magnetic energy is released and translated through turbulence [3–11] in LTSTMR.

It is now clear that MR in a weak 3D setting is different from the 2D/2.5D case, although most of the literature on reconnection focuses on the 2D/2.5D problem due to their theoretical and computational simplifications (Supplementary videos 1 ∼ 2).

In the 3D MR model, MR can occur at null points, separators or quasi-separators instead of the 2D *X*-type null points, which allows us to investigate the effect of the magnetic fluctuation-induced self-generating-organization and the plasma turbulence-induced self-feeding-sustaining in the diffusion region from the 3D temporal-spatial scale [12–16].

As for the second part of this two-paper series, this paper investigates the role of turbulence in the evolution of the 3D magnetic helical structures (flux ropes) with RHPIC-LBM from the continuous kinetic-dynamic-hydro fully coupled temporal-spatial scale on the ***Tianhe-2*** supercomputer platform from National Supercomputer Center in Guang Zhou (NSCC-GZ).

The physical-mathematical model and numerical implementation of RHPIC-LBM for the 3D LTSTMR turbulent flux rope interaction in the relativistic resistive Magnetohydrodynamics (MHD) diffusion region are summarized in Section 2 and Section 3, respectively.

Based on the simulation evidence, the turbulence of the magnetic helical structure, the turbulence of the current density vector fields, the turbulence of the magnetic fields' self-generating-organization, the turbulence of the plasma motion self-feeding-sustaining, and the turbulence acceleration mechanism of the ions and electrons are investigated in Section 4.

Finally, the conclusion and concluding remarks are summarized in Section 5.

List of symbols

r_e	The *Larmor* radius
d_e	The electron inertial length
Ω_{ce}	The electron gyroperiod
α_j	Degree of ionization, the indices $j = e, i$ denote electron and ions, respectively.
n	The number density
q	Charge of particles
m_α	The rest mass of particle
$\boldsymbol{U}$	The plasma relativistic velocity
$\boldsymbol{B}$	The magnetic fields strength
$\boldsymbol{E}$	The electric fields strength
$\boldsymbol{p}$	The relativistic momentum
c	Speed of light
t	Time
ε_0	The vacuum permittivity
n_α	The number density of particles
K	Boltzmann constant
T_{th}	Temperature of the thermal bath
f^α	The relativistic distribution functions
$\boldsymbol{B}_0$	Magnetic field at the inflow boundary
$\boldsymbol{B}_g$	Relative magnitude of the imposed guide field
$\vec{u}_{dj}$	Drift velocities in the current direction, the indices $j = e, i$ denote electron and ions, respectively.
$\vec{u}_{de}$	Electron drift velocities in the current direction
T_e	The electron temperatures
T_i	The ion temperatures
$R_{0,j}$	Thermal *Larmor* radius, the indices $j = e, i$ denote electron and ions, respectively.
$\boldsymbol{b}$	The unit vector parallel to $\boldsymbol{B}$

Greek

$\alpha = 1, 2$	Represents ion and electron, respectively.
β	The ratio of the plasma pressure to the magnetic pressure
η	The plasma resistivity
τ_e	The electron collision time
λ	The Half thickness of the initial electron current
χ	The unit time-to-relaxation time ratio

Subscripts

$\boldsymbol{V}$	Refer to the velocity of charged particle
e	Refer to the electron
i	Refer to the ion
n	Refer to the neutral particle/flow

Superscripts

Par($\parallel$)	Refer to components parallel to B
perp ($\parallel$)	Refer to components perpendicular to B
e	Refer to the electron particle
i	Refer to the ion particle
n	Refer to the neutral particle
–	Refer to the average component of a vector
$\sim$	Refer to the fluctuation (magnetic field) or turbulence (plasma motion) component of a vector

2. Physical and mathematical model

For corona and solar terrestrial spaces LTSTMR problems (e.g., solar limb, flare, CME, solar wind, Earth ionosphere-magnetospheres), if we assume that the degree of ionization is equal to 1 ($\alpha_e = \frac{n_e}{n_e+n_n} \approx 1,\ \alpha_i = \frac{n_e+n_i}{n_e+n_i+n_n} \approx 1$), and the plasma pressure is much smaller than magnetic pressure ($\beta = \frac{p}{p_{mag}} = \frac{2\mu_0 n K_B T}{B^2}$), then the MR in solar corona atmosphere activities and solar terrestrial spaces can be considered as a typical full ionized LTSTMR problem.

Since the solar corona is dominated by hydrogen, we neglect helium, oxygen and other chemical compositions in the present kinetic-dynamic-hydro fully coupled temporal-spatial scale 3D LTSTMR model [17,18]; the number density of hydro-

Table 1
The explosive astronomical & astrophysical phenomena [1,2].

Phenomena	Energy (erg)	Evolution time
Formation of a massive black hole	10^{62}	Myr
Merging of stellar mass black holes	10^{56}	1s
Gamma ray burst (GRB)	10^{54}	10s
Merging of neutron stars	10^{54}	1s
Blazar flare (acceleration disk, jet)	10^{53}	1day
Tidal disruption of a star by a BH	10^{53}	1day
Super novae (including neutrino)	10^{53}	1s
Magnetar flare	10^{47}	0.1s
Pulsar nebulae flare	10^{41}	day
Fast radio burst (FRB)	10^{39}	1 min
Protostellar flare	10^{36}	hour
Solar flare	10^{31}	100s

Table 2
Summary of observations of various flares [1,2].

Flare type	Flare size (Km)	Life time (t)	Alfvén time (t_A)	Mass ejection
Micro-	$10^3 \sim 10^4$	$100 \sim 1000\,\mathrm{s}$	$1 \sim 10\mathrm{s}$	jet/surge
Impulsive-	$(1 \sim 3) \times 10^4$	$10m \sim 1\,\mathrm{h}$	$10 \sim 30\mathrm{s}$	x-ray plasmoid
Impulsive-	$(1 \sim 3) \times 10^4$	$10m \sim 1\,\mathrm{h}$	$10 \sim 30\,\mathrm{s}$	x-ray spray
Long duration (LDE)	$(3 \sim 10) \times 10^4$	$1 \sim 10\,\mathrm{h}$	$30 \sim 100\,s$	x-ray plasmoid
Long duration (LDE)	$(3 \sim 10) \times 10^4$	$1 \sim 10\,\mathrm{h}$	$30 \sim 100\,\mathrm{s}$	prom eruption
Giant arcades	$10^5 \sim 10^6$	$10h \sim 2d$	$100 \sim 1000\,\mathrm{s}$	CME
Giant arcades	$10^5 \sim 10^6$	$10h \sim 2d$	$100 \sim 1000\,\mathrm{s}$	prom eruption

gen, n_{n_h}, can be assumed to be equal to the solar corona number density, n_n. We analyze the magnetic energy conversion, plasma heating, charged particles energization and acceleration from the RHPIC-LBM simulation results with the observation input parameters and variables [19–27].

Then, the governing formulation of the RHPIC-LBM model for resistive relativistic MHD can be rewritten as,

$$\frac{\partial f^\alpha}{\partial t} + \frac{1}{\varepsilon^\alpha}\boldsymbol{U}^\alpha \cdot \nabla_x f^\alpha + \left(\frac{1}{\varepsilon^\alpha}\boldsymbol{E} + (\delta^\alpha)^2 \boldsymbol{U}^\alpha \times \boldsymbol{B}\right) \cdot \frac{\partial f^\alpha}{\partial \boldsymbol{p}^\alpha} = \frac{\theta^\alpha}{(\varepsilon^\alpha)^2}\nabla_{\boldsymbol{p}^\alpha} \cdot \left(\nabla_{\boldsymbol{p}^\alpha} f^\alpha + \boldsymbol{U}^\alpha f^\alpha\right), \tag{1}$$

where $\alpha = 1, 2$ represents the ion and electron, respectively. $\varepsilon^\alpha = q^2 c^{-1} \varepsilon_0^{-1} n_\alpha (KT_{th} + 2m_\alpha c^2)^{1/2} (KT_{th})^{-3/2}$, $\delta^\alpha = (1 + 2m_\alpha c^2/KT_{th})$, and $\theta^\alpha = \chi \varepsilon^2$ are three dimensionless parameters.

The parameters and variables q, m_α, $\boldsymbol{U}$, $\boldsymbol{B}$, $\boldsymbol{E}$, $\boldsymbol{p}$, t, c ε_0, n_α, K, T_{th}, χ and f^α represent the charge of the particles, the rest mass of the particle, the plasma's relativistic velocity, the strength of the magnetic field, the strength of the electric field, the relativistic momentum, time, the speed of light, the vacuum permittivity, the number density of the particles, Boltzmann constant, the temperature of the thermal bath, the unit time-to-relaxation time ratio and the relativistic distribution functions, respectively.

The four-vector of the relativistic plasma motion, $\boldsymbol{U}$, and the four-vector of the relativistic momentum, $\boldsymbol{p}$, can be rewritten as,

$$(\boldsymbol{U}^\alpha) = \left(\frac{dx^\alpha}{d\tau}\right) = (c\gamma, \vec{\boldsymbol{u}^\alpha}\gamma) \tag{2}$$

$$(\boldsymbol{p}^\alpha) = (m_\alpha \boldsymbol{U}^\alpha) = (m_\alpha c\gamma, m_\alpha \vec{\boldsymbol{u}}\gamma) = (\boldsymbol{p}^{\alpha 0}, \vec{\boldsymbol{p}}^\alpha), \tag{3}$$

where τ, $\gamma = (1 - |\vec{\boldsymbol{u}}|^2/c^2)^{-1/2}$, $\vec{\boldsymbol{u}}(u_1, u_2, u_3)$, $\boldsymbol{p}^0$ and $\vec{\boldsymbol{p}}(p_1, p_2, p_3)$ represent the proper time, Lorentz factor, the plasma's velocity, and the 1^{st} component of $\boldsymbol{p}$ and the momentum, respectively [28–31].

Since the fluctuation in magnetic self-generating-organization and the turbulence in plasma motion self-feeding-sustaining in the diffusion region belong to a full developed nonlinear case, the dynamics comprises many interacting degrees of freedom.

Thus, it is necessary to consider the joint contribution of electron-MHD (EMHD, microphysics), Hall physics (HMHD), ion-MHD (IMHD, macrophysics) and the large hydroscale (hydrophysics) from the theory of continuous kinetic-dynamic-hydro fully coupled temporal-spatial turbulence instead of the classical theory of MHD turbulence [10,32–35].

To quantitatively distinguish the effect of the mean turbulence components (macro scale: flux rope, plasmoid bubbles and MHD waves) and pulsating components (micro scale: flux rope, plasmoid bubbles and kinetic waves), which are beyond the quasilinear approximation and ideal MHD frozen-in condition [36,37], the relativistic plasma motion ($\boldsymbol{U}$), the magnetic field ($\boldsymbol{B}$) and the electric field strength ($\boldsymbol{E}$) are decomposed into the average components ($\bar{\boldsymbol{U}}, \bar{\boldsymbol{B}}, \bar{\boldsymbol{E}}$) and the fluctuation components ($\tilde{\boldsymbol{U}}, \tilde{\boldsymbol{B}}, \tilde{\boldsymbol{E}}$).

From mean field theory, we can use the average components and the fluctuation components to describe the macrodynamic scale flow characteristics and the small-kinetic scale particles characteristics of the plasma, respectively.

Then, the full-blown magnetic induction equation for the entire resistive relativistic MHD simulation domain can be written as [5,38–43],

$$\frac{\partial \bar{\boldsymbol{B}}}{\partial t} = \nabla \times \left(\bar{\boldsymbol{U}} \times \bar{\boldsymbol{B}}\right) - \nabla \times \left(\hat{\alpha}\bar{\boldsymbol{B}}\right) + \hat{\beta}\nabla^2\bar{\boldsymbol{B}} + \eta_s\nabla^2\bar{\boldsymbol{B}} \tag{4}$$

$$\frac{\partial \tilde{\boldsymbol{B}}}{\partial t} = \nabla \times \left(\bar{\boldsymbol{U}} \times \tilde{\boldsymbol{B}}\right) + \nabla \times \left(\tilde{\boldsymbol{U}} \times \bar{\boldsymbol{B}}\right) + \nabla \times \left(\tilde{\boldsymbol{U}} \times \tilde{\boldsymbol{B}}\right) - \nabla \times \left(\hat{\alpha}\bar{\boldsymbol{B}}\right) + \hat{\beta}\nabla^2\bar{\boldsymbol{B}} + \eta_s\nabla^2\tilde{\boldsymbol{B}} \tag{5}$$

where $\hat{\alpha} = \frac{\hat{\alpha}_0 + (\tau_c/3\rho\eta_s)(\hat{\beta}\bar{\boldsymbol{J}}\cdot\bar{\boldsymbol{B}} + \langle\tilde{\boldsymbol{E}}\cdot\tilde{\boldsymbol{B}}\rangle)}{1+(\tau_c/3\rho\eta_s)\bar{\boldsymbol{B}}^2}$, $\hat{\beta} = \frac{\tau_{\hat{\beta}}\langle\tilde{\boldsymbol{U}}\cdot\tilde{\boldsymbol{U}}\rangle}{3}$, $\hat{\alpha}_0 = \frac{\tau_c\langle\tilde{\boldsymbol{U}}\cdot\nabla\times\tilde{\boldsymbol{U}}\rangle}{3}$. $\hat{\alpha}$, $\hat{\beta}$, τ_c, $\tau_{\hat{\beta}}$, η_s, ρ and $\hat{\alpha}_0$ represent the parameter amplified seed magnetic field ($\hat{\alpha}$-effect), the parameter-enhanced diffusion rate ($\hat{\beta}$-effect), the approximate eddy correlation time far enough away from neutral line, the approximate eddy correlation time near the neutral line, classical resistivity, density of the electron and the parameter amplified seed magnetic field ($\hat{\alpha}_0$-effect), respectively.

The full-blown magnetic induction equation of the resistive magnetic fluctuation-induced self-generating-organization in the plasma turbulence-induced self-feeding-sustaining diffusion simulation domain, which is around the neutral region, can be written as [5,38–43],

$$\frac{\partial \boldsymbol{B}}{\partial t} = \nabla \times \left\{ \begin{array}{l} \underset{(a)}{\frac{m_e}{e}\frac{\partial \boldsymbol{U}_e}{\partial t}} + \underset{(b)}{\frac{m_e}{e}(\boldsymbol{U}_e\nabla)\boldsymbol{U}_e} + \underset{(c)}{\frac{1}{en_e}\nabla P_e} + \underset{(d)}{\frac{1}{en_e}\nabla \boldsymbol{\pi_e}} + \underset{(e)}{\frac{m_e}{e}\langle\xi\cdot\nabla\cdot\xi\rangle} + \underset{(f)}{\boldsymbol{U}_e\times\boldsymbol{B}} - \underset{(g)}{\alpha_\parallel(\boldsymbol{J}\cdot\boldsymbol{b})\boldsymbol{b}} \\ \underset{(h)}{-\alpha_\perp\boldsymbol{b}\times(\boldsymbol{J}\times\boldsymbol{b})} + \underset{(i)}{\alpha_\Lambda(\boldsymbol{b}\times\boldsymbol{J})} + \underset{(j)}{\frac{\beta_\parallel}{e}(\nabla T_e\cdot\boldsymbol{b})\boldsymbol{b}} + \underset{(k)}{\frac{\beta_\perp}{e}\boldsymbol{b}\times(\nabla T_e\times\boldsymbol{b})} + \underset{(l)}{\frac{\beta_\Lambda}{e}(\boldsymbol{b}\times\nabla T_e)} + \underset{(m)}{\left\langle\xi\times\tilde{\boldsymbol{B}}\right\rangle} \end{array} \right\} \tag{6}$$

where m_e, e, $\boldsymbol{U_e}$, n_e, $P_e = n_eKT_e$, T_e, $\xi = \frac{e\tilde{\boldsymbol{E}}}{\omega_e m_e}$, $\boldsymbol{b}$, $\alpha_\parallel$, $\alpha_\perp$, α_Λ, $\beta_\parallel$, $\beta_\perp$, β_Λ and $\boldsymbol{J}$ represent the mass of the electron, the electric charge, the electron velocity, number density of the electrons, the electron pressure, the temperature of electron, displacement of the electron closely linked with the high-frequency components of the electron's velocity, the unit vector in the direction of the magnetic field, the electrical resistivity parallel to $\boldsymbol{b}$, the electrical resistivity perpendicular to $\boldsymbol{b}$, the electrical resistivity in the $\boldsymbol{b}\times\nabla T_e$ direction, the thermoelectric tensor parallel to $\boldsymbol{b}$, the thermoelectric tensor perpendicular to $\boldsymbol{b}$, the thermoelectric tensor in the $\boldsymbol{b}\times\nabla T_e$ direction and the current density, respectively.

The Maxwell equation corresponding to Eq. (1) can be written as,

$$\begin{cases} \partial_t\boldsymbol{E}(t,\boldsymbol{r}) - \nabla\times\boldsymbol{B}(t,\boldsymbol{r}) = -\frac{j_e}{\varsigma_e} + J_b \\ \varsigma_e^2\delta_e^2\partial_t\boldsymbol{B}(t,\boldsymbol{r}) + \nabla\times\boldsymbol{E}(t,\boldsymbol{r}) = 0 \\ \nabla\cdot\boldsymbol{E}(t,\boldsymbol{r}) = -\rho_e + D_b \end{cases} \tag{7}$$

$$\begin{cases} \partial_t\boldsymbol{E}(t,\boldsymbol{r}) - \nabla\times\boldsymbol{B}(t,\boldsymbol{r}) = -\frac{j_i}{\varsigma_i} + J_b \\ \varsigma_i^2\delta_i^2\partial_t\boldsymbol{B}(t,\boldsymbol{r}) + \nabla\times\boldsymbol{E}(t,\boldsymbol{r}) = 0 \\ \nabla\cdot\boldsymbol{E}(t,\boldsymbol{r}) = \rho_i + D_b \end{cases} \tag{8}$$

where j_e, j_i, ρ_e, ρ_i, J_b and D_b represent the electron (species I charged particle) motion-induced current density, the ion (species II charged particles) motion-induced current density, the electron number density, the ion number density, the background current density, and the background charge density, respectively [44].

Combined with Eqs. (1 ∼ 8), the role of turbulence in the magnetic self-generating-organization ($\nabla\tilde{\boldsymbol{B}}$, $\nabla\times\tilde{\boldsymbol{B}}$), and the plasma self-feeding-sustaining ($\nabla\tilde{\boldsymbol{U}}$, $\nabla\cdot\tilde{\boldsymbol{U}}$, $\nabla\times\tilde{\boldsymbol{U}}$) in the diffusion region can be translated into the interaction between RHPIC-LBM lattice grid of the field's virtual flow and the RHPIC-LBM lattice grid of the plasma's motion.

The contribution of the mean components ($\bar{\boldsymbol{B}}, \bar{\boldsymbol{U}}, \bar{\boldsymbol{E}}$) induced dynamic-hydro resistivity $\eta_h(\nabla\bar{\boldsymbol{B}}, \bar{\boldsymbol{U}})$, the fluctuation components ($\tilde{\boldsymbol{B}}, \tilde{\boldsymbol{U}}, \tilde{\boldsymbol{E}}$) induced kinetic resistivity $\eta_k(\nabla\tilde{\boldsymbol{B}}, \nabla\times\tilde{\boldsymbol{B}}, \nabla\tilde{\boldsymbol{U}}, \nabla\cdot\tilde{\boldsymbol{U}}, \nabla\times\tilde{\boldsymbol{U}})$, and the *Spitzer* resistivity (η_s) to the magnetic conversion, plasma heating and particle acceleration in the diffusion region can be investigated in the present RHPIC-LBM, which is ignored in the pervious hybrid acceleration simulation model.

Before quantitatively analyzing the role of turbulence in the magnetic fields self-generating-organization, plasma turbulent self-feeding-sustaining process with a mathematical model and numerical implementation, some parameters/variables must be defined in the whole nonideal resistive MHD domain and in the local resistive domain.

Due to the coupling of the magnetic field strength ($\boldsymbol{B}$) and plasma motion ($\boldsymbol{U}$), especially for the fluctuation component ($\tilde{\boldsymbol{B}}$) and the turbulence components ($\tilde{\boldsymbol{U}}$), there is strong coherence between $\tilde{\boldsymbol{B}}$ and $\tilde{\boldsymbol{U}}$ that leads to the turbulence-induced electric fields, $\boldsymbol{E} = \left\langle\tilde{\boldsymbol{U}}\times\tilde{\boldsymbol{B}}\right\rangle$, which are not equal to zero.

At this time, the first-order smoothing and quasilinear approximation is no longer applicable; $\bar{\boldsymbol{U}}$ is a function of time, t, and space, $x_i(i = 1\sim 3)$, while there are nonconstant values at all kinetic-dynamic-hydro temporal-spatial scales, and $\tilde{\boldsymbol{U}}$ becomes an anisotropic vector in the diffusion region.

When the temporal-spatial scale of the fluctuation ($\tilde{\boldsymbol{B}}$) and turbulence ($\tilde{\boldsymbol{U}}$) reduce and reach the temporal-spatial scale of the diffusion region, the components $\tilde{\boldsymbol{U}}\times\tilde{\boldsymbol{B}} - \langle\tilde{\boldsymbol{U}}\times\tilde{\boldsymbol{B}}\rangle$, $\hat{\beta}\nabla^2\tilde{\boldsymbol{B}}$, $\eta_s\nabla^2\tilde{\boldsymbol{B}}$ in Eq. (5) cannot be neglected.

$\hat{\alpha}$ and $\hat{\beta}$ can be decomposed into average components ($\bar{\hat{\alpha}}$, $\bar{\hat{\beta}}$) and fluctuation components ($\tilde{\hat{\alpha}}$, $\tilde{\hat{\beta}}$). Their explicit expression can be rewritten as,

$$\tilde{\hat{\alpha}} = \frac{(\tau_c/3\rho\eta_s)(\hat{\beta}(\nabla\times\bar{\boldsymbol{B}})\cdot\bar{\boldsymbol{B}} + \langle\bar{\boldsymbol{E}}\cdot\bar{\boldsymbol{B}}\rangle)}{1+(\tau_c/3\rho\eta_s)\bar{\boldsymbol{B}}^2} \tag{9}$$

$$\bar{\hat{\alpha}} = -\frac{\tau_c}{3}\langle\tilde{U}\cdot(\nabla\times\tilde{U})\rangle \tag{10}$$

$$\bar{\hat{\beta}} = \tilde{\hat{\beta}} = \frac{\tau_{\tilde{\hat{\beta}}}\langle\tilde{\boldsymbol{U}}\cdot\tilde{\boldsymbol{U}}\rangle}{3} \tag{11}$$

By combining Eq. (6) and Eqs. (9 ∼ 11), we can explore the interaction of flux ropes-to-plasmas bubbles, plasmas bubbles-to-plasmas bubbles, and flux ropes-to-flux ropes at same time, and determine the turbulence role in self-generating-organization magnetic fields in the self-feeding-sustaining plasma diffusion region. Then, we can understand the mechanism of turbulence in the flux rope interaction.

3. Numerical implementation

3.1. Initial discrete distribution functions

Selecting the initial RHPIC-LBM lattice grid in geometrical coordinates and momentum coordinates for $f^{\alpha}(\boldsymbol{x},\boldsymbol{p},t)$ is the first step to establish the initial geometry and topology structure of the magnetic field in the entire simulation domain.

In part I of this series, we used random, semirandom and several uniform discrete distributions as the initial discrete distribution function to test and validaed the RHPIC-LBM numerical implementation and code.

In this paper, the $D^{\alpha\_eq}3Q19$ equilibrium Maxwell-Jüttner discrete distribution function for relativistic ion and electron particles in continuum temporal-spatial space is used as the initial load to the RHPIC-LBM lattice grid in the 3D LTSTMR magnetic helical structures evolution simulation case, which can be written as [45–49],

$$f_{\xi}^{\alpha\_eq}(\boldsymbol{x},\boldsymbol{p},t) = \frac{3c_0^{\alpha 2}(\varepsilon_0^{\alpha}+p^{\alpha})\omega_{\xi}{}^{\alpha}}{4c_t^{\alpha}}\left\{\begin{matrix} 1+c_a^{\alpha x}c_a^{\alpha y}\chi_a^{\alpha x}\chi_a^{\alpha y}+c_a^{\alpha x}c_a^{\alpha z}\chi_a^{\alpha x}\chi_a^{\alpha z}+c_a^{\alpha y}c_a^{\alpha z}\chi_a^{\alpha y}\chi_a^{\alpha z}+\\ (\frac{c_t^{\alpha}\chi^{\alpha 0}}{2c^{\alpha 2}}-\frac{\chi^{\alpha 0}}{\nu^{\alpha}c^{\alpha 0}})(\vec{c}_{\alpha a}^{\,j}\cdot\vec{\chi}^{\alpha})\\ +\frac{4}{15}[(c_a^{\alpha x}\chi^{\alpha x})^2+(c_a^{\alpha y}\chi^{\alpha y})^2+(c_a^{\alpha z}\chi^{\alpha z})^2-\frac{4}{\nu^{\alpha}}(\vec{\chi}^{\alpha}\cdot\vec{\chi}^{\alpha})]\end{matrix}\right\} \tag{12}$$

For more detailed parameter information in Eq. (12), please refer to part I paper of this two-paper series.

Setting Eq. (12) as the initial load for the RHPIC-LBM lattice grid configuration can reduce the fluctuation levels that were created from the discrete process, which is one of the manners to control and reduce the physical error limit.

3.2. Self-consistency in extended particles interaction/collision

Smooth the extended particles' interaction/collision process in the entire simulation domain can also reduce the physical error limit from the discrete particles' effects.

In RHPIC-LBM, we use a pseudoparticle (one RHPIC-LBM lattice grid includes at least two different pseudoparticles), a superparticle (one pseudoparticle includes many superparticles), and a real charged particle (wherein each superparticle represents a set of many real particles) to control this type physical error limit.

The tests and benchmarks in Part I show that when $N\cdot\Delta x/\sigma$ is sufficiently small, the development of microscale fluctuations can be eliminated.

In the present paper, the simulation domain is distributed in the massively parallel computation following a 4D domain decomposition, which assigns real super particles extended superparticles (magnetic field, electric field and electromagnetic field) with 2^{14} lattice grids and 2^{10} lattice grids, respectively.

We also use the Hurst index to control and reduce this value under different temporal-spatial scales in the real simulation process.

3.3. System error accumulation

In the 3D MR simulation, the system error accumulation is composed of numerical stabilities, GALGR and PALGR error accumulation, truncation and roundoff error accumulation.

In the RHPIC-LBM code, we use higher (e.g., second order) expansions of the discrete distribution function in the temporal-spatial space, which automatically increase the RHPIC-LBM lattice grid number and decrease the RPHIC-LBM lattice grid size (GALGR for the geometric simulation domain and PALGR for the physical physical simulation domain, in which the parameters'/variables' gradients drastically change sites) to reduce the system error.

The tests and benchmarks in Part I show that when $\frac{\Delta x}{c\Delta t}\geq 0.2$, the development of numerical instabilities can be controlled at a low oscillatory state, which is much lower than the Kinetic Alfvén velocity (KAV) and the Kinetic Alfvén wave(KAW) velocity, and the low entropy and conservation of energy is still in good physical condition in the simulation.

3.4. Initial magnetic configuration

In Part I of the series, we used a double Harris-type, multi Harris-type and single Harris-type as the initial magnetic configuration for testing and validation of the RHPIC-LBM code.

In the present 3D simulation, the initial equilibrium of the magnetic field is given by Bacecher and P. Kuska [50–52],

$$\boldsymbol{B} = B_0 \tanh\left(\frac{z}{\lambda}\right) \cdot \vec{i} + B_0 \sqrt{B_g^2 + \operatorname{sech}^2\left(\frac{z}{\lambda}\right)} \cdot \vec{j} + B_g \cdot \vec{k} \tag{13}$$

$$\lambda = \sqrt{\frac{K_B \cdot (T_e + T_i)}{2\pi n_0 q^2}} \cdot \frac{c}{u_{di} - u_{de}} = 2 \cdot R_{0,e} \cdot \frac{v_{te}}{u_{de}} \tag{14}$$

$$B_0 = \sqrt{8\pi \cdot n_0 \cdot K_B \cdot (T_e + T_i)}, \tag{15}$$

where B_0, B_g, λ, u_{de}, u_{di}, T_e, and T_i represent the magnetic field at the inflow boundary, the relative magnitude of the imposed guide field, the half thickness of the initial electron CS [33,53], the electron drift velocity in the current direction, the ion drift velocity in the current direction, the electron temperature and the ion temperature, respectively.

3.5. Input parameters and IC/BC definition

As for the initial condition in the geometric and physical simulation domain of the present 3D flux rope turbulence evolution case, the electron CS with peak density n_0 superimposed on a uniform background density $n_b = 0.05 \times n_0$ is set up in 3D space with $x \times y \times z = 16{,}000 \times 32{,}000 \times 16{,}000$ lattice girds.

The total number of superparticles is $8000 \times 16{,}000 \times 8000 \times 2^{\hat{n}}$, where $\hat{n} \geq 8$ and depends on the number density of the background. The open boundary condition is assumed in the x and y directions.

The initial magnetic configuration in Eq. (13) is normalized [50–52,54] and the simulation results are presented in normalized units.

No magnetic fluctuation and plasma turbulence seed is imposed initially, and all runs were performed using *964,000* $\sim$ *100,000* cores of the supercomputer *Tianhe-2* from NSCC-GZ.

The other input parameters and IC/BC are the same as the 2.5D LTSTMR in Part I of this series.

4. Analysis of the role of turbulence in the flux rope interaction of 3D LTSTMR

4.1. Turbulence of a magnetic helical structure

In the 2D/2.5D model, to investigate the turbulence evolution of the magnetic geometry and topology in the diffusion region, we defined the magnetic island as a kind of magnetic field structure consisting of a bipolar magnetic field normal to the CS, with an enhancement of the core field in the axial direction with a compressed and high-temperature plasma inside of it [55,56].

While the magnetic configuration change at the resistive diffusion region is 3D in the natural real LTSTMR, the initial small magnetic helical perturbation, $(\tilde{B}_x, \tilde{B}_y, \tilde{B}_z)$, will change the geometry and topology of the magnetic field, making the magnetic field lines (MFLs) orthogonal to the vector of the perturbation $\tilde{\boldsymbol{B}}$, forming a magnetic helical structure upon the flux surface (consisting of many spiral magnetic field lines).

In the present 3D LTSTMR simulation, we define the magnetic topology structure as consisting of twisted MFLs and filling the spiral null points as the flux rope, which is a magnetic helical structure, and the magnetic island structure is the projection of the flux rope structure in two dimensions.

The 2D/2.5D MR during the formation, shrinking and breakup of the magnetic islands of the microkinetic stage, the 2D/2.5D MR during the merging/coalescence and growth of the magnetic islands of the cross-scale coupled microkinetic & macrodynamic stage, and the magnetic islands reaching constant sizes and eruptions with the Alfvén speed of the cross-scale coupled macrodynamic & large-hydro stage will undergo turbulence evolution of the flux ropes in the continuous kinetic-dynamic-hydro fully coupled temporal-spatial scale in the magnetic fluctuation-induced self-generating-organization region and the plasma turbulence-induced self-feeding-sustaining region in the 3D MR.

Observations of regions with solar atmosphere activities show that the flux rope emergence and formation, mass draining, near-surface reconnection and the interaction with the surrounding fields will appear in the chromospheric-corona reconnection region [57–61], and MRs can occur in the absence of null points [12–16]. Demoulin et al. [62] introduced concept of quasi-separatrix layers (QSLs) in the 3D MR in a solar flare; Guo et al. [19] and Chen et al. [20] found slipping reconnection (QSLs-induced MR) phenomena in the sun flare; and Gekelman and Lawence observed QSLs phenomena in their experiments [63,64].

However, due to the limitation of the original algorithm and a super computer resource, until now there has been no evidence from simulations that can verify these phenomena in 3D MR, even if there are many 3D theoretical models have been developed [12–16].

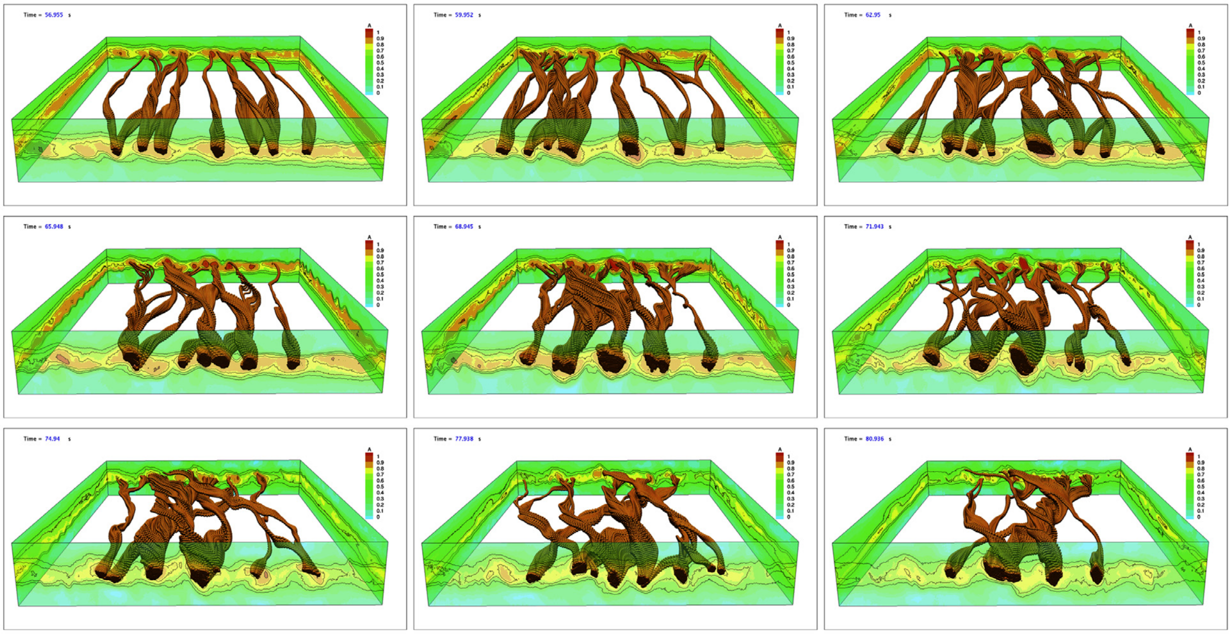

Fig. 1. Evolution of flux ropes topology structure in the self-generation stage ($\sim$ 56.955 s), in the self-generating-organization stage (56.955 s–59.952 s), in the self-organization stage (59.952 s–68.945 s), and in the full-developed nonlinear chaos-turbulence stage (68.952 s–80.936 s). The black curves show the magnetic potential projected onto the *xz* planes and *xy* planes

In this section, the MFLs continuous exchange connectivities with their neighbor-induced slipping MR [65–73] (composited of torsional spin MR, torsional fan MR and spine-fan MR) and the MFLs break-rejoin-induced MR in the evolution of the magnetic helical structure's turbulence is investigated (Fig. 1).

In this paper, we define the slipping MR and MFLs break-rejoin-induced MR as 1st type MR and 2nd type MR, respectively.

Simulation evidence shows that the initial fluctuation component ($\tilde{B}_x, \tilde{B}_y, \tilde{B}_z$) induced magnetic fields turbulence is not isotropic, which leads to anisotropic turbulence behavior of the magnetic potential vector ($\boldsymbol{A}$) in the 3D temporal-spatial scale.

The hyperbolic separator exists in the quasilinear region of the flux ropes formation, and the elliptic separator exists in the flux rope network and sub flux rope evolution of the nonlinear fully developed region.

We selected two different moments (56.955 s and 77.938 s) from Fig. 1, enlarging the fine structures evolution of the flux ropes in the mixed oblique and tearing-kink instabilities sites, and investigated the flux rope turbulence features under a quasilinear stage (Fig. 2) and (fully developed the nonlinear stage (Fig. 3).

As shown in Figs. 2 and 3, all the torsional spine MRs, torsional fan MRs and spine-fan MRs belong to the 1st type MR and form spiral null points (in space physics, researchers also define these as *O*-type null points [21,22]).

The resistive diffusion sites of these MRs are always located in the adjacent MFLs compress-stretch-slip areas ($\nabla\tilde{\boldsymbol{B}} >> 1$), and the magnetic energy conversion in these sites (1st type MRs with *O*-type null points) does not depend on the MFLs break-rejoin process, which is completely different from the original 2D/2.5D MR model.

Certainly, the MFLs break-rejoin-induced 2nd type MRs also exist in the resistive diffusion region, forming *X*-type null points, and converting energy from magnetic into plasma as these sites (2nd type MRs with *X*-type null points).

Numerical simulation show that the 1st type MR plays the leading role in the entire turbulence evolution (both the linear and nonlinear stages), while the 2nd type MR plays a less important role even though its role in the magnetic release-conversion becomes stronger after the turbulence evolution enters into the full developed nonlinear stage.

Compared with the quasilinear (Fig. 2) and (fully coupled nonlinear (Fig. 3) turbulence stages, we can see that the 2nd order and smaller *n*th order sub flux ropes structure appear and form flux ropes networks in the nonlinear stage, which means that the full development of the magnetic turbulence improves the efficiency of the magnetic energy release-conversion.

The 1st type MR will generate a higher resistivity from the flux ropes hybrid instabilities (mixed tearing and oblique instabilities) and wave-particle interactions (turbulence acceleration), which can explain the phenomena where the predicted reconnection rates from the 2D/2.5D model are much slower than the observations.

In the present 3D simulation, the mixed tearing and oblique instabilities are created by the initial fluctuation component in the *x* direction ($\tilde{B}_x$) and in the *z* direction ($\tilde{B}_z$), respectively, while the oblique instabilities (in macro MHD simulations, some researchers also define them as tilt instabilities [74–76]) induced from $\tilde{B}_z$ cannot be reflected in the original 2D/2.5D MR model.

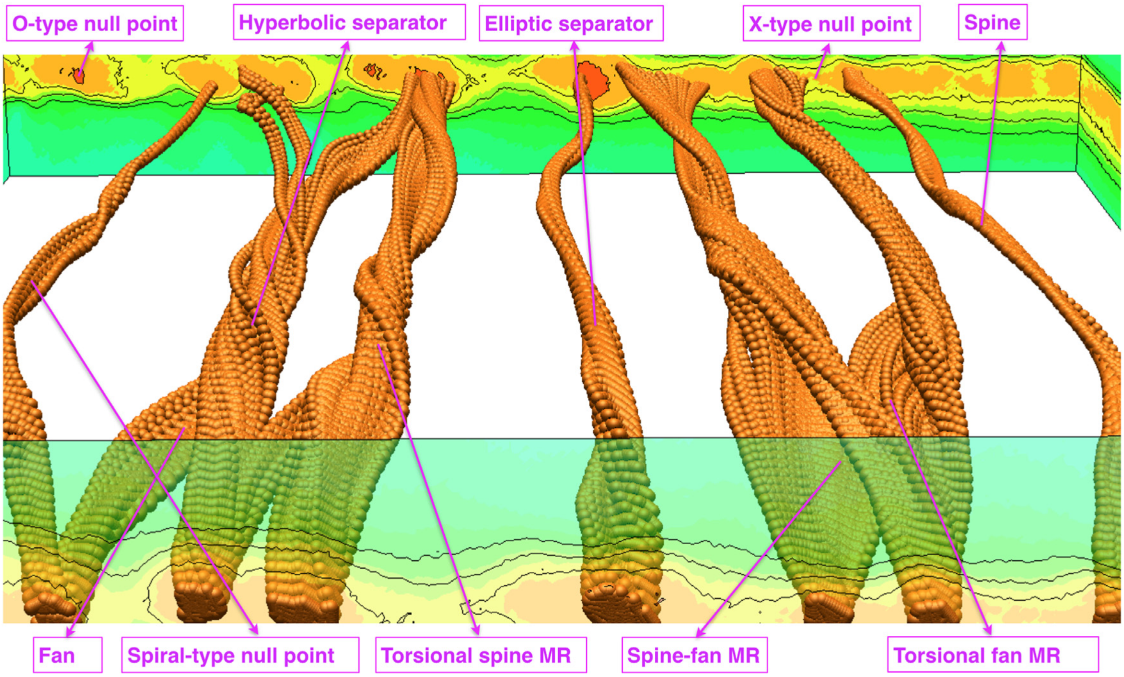

Fig. 2. Topology and evolution of the magnetic flux rope under the quasilinear stage at 56.955 s

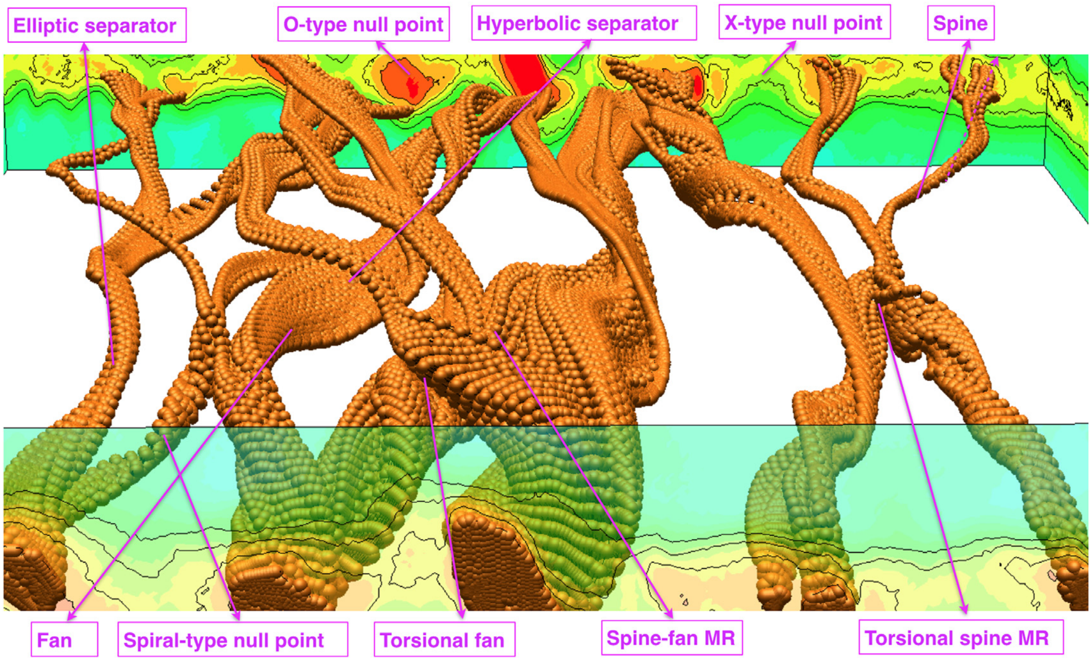

Fig. 3. Topology and evolution of the magnetic flux rope under the nonlinear stage at 77.938 s

Figs. 1–3 show that the initial fluctuation $\tilde{B}_z$ induced $\nabla\tilde{\boldsymbol{B}}$ leads to the changes in the magnetic topology structure, forms a slipping MR, and translates the magnetic energy into plasma energy through a flux rope emergence-destabilizations process.

This why our 2.5D RHPIC-LBM work in Part I can determine that the initial magnetic field perturbation ($\tilde{B}_z$) will make $\nabla\tilde{\boldsymbol{B}}$ increase in the front of the adjacent magnetic island's mergence region (Section 4.5 in Part of the series, Supplementary videos 3–5). However, it cannot answer whether a large magnetic gradient ($\nabla\tilde{\boldsymbol{B}}$) will contributes to the magnetic energy release-translation [80].

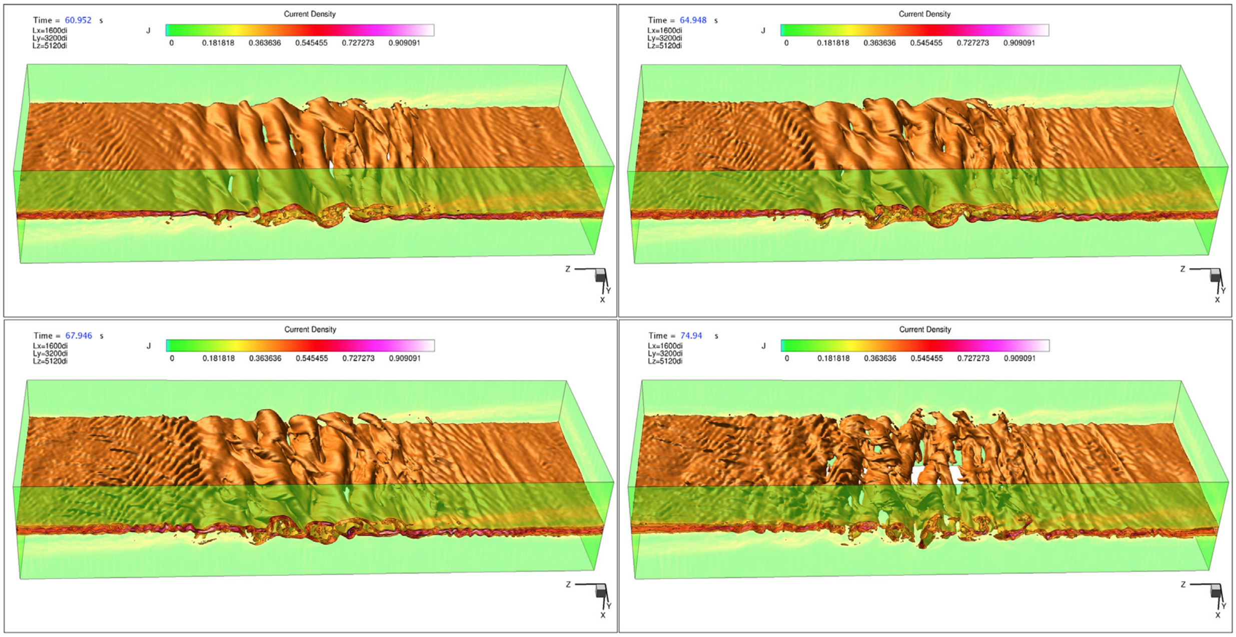

Fig. 4. Topology of the current density $\boldsymbol{J}(J_{\|}, J_{\perp})$ evolution in the diffusion regions from 60.952 s–74.94 s

4.2. Turbulence of current density vector fields

4.2.1. Topology and evolution of current density vector fields

In the above section, we determined the spine-fan magnetic topology structures as well as the 1st and 2nd type MR in the turbulence flux ropes interaction.

For the convenience of analyzing the role of the mixed MR (1st type and 2nd type) in the energy transportation diffusion region, the elliptic (*O*-type) separator, the hyperbolic (*X*-type) separator, the generic fan-fan separator (X-type) and the isolated 3D null points (O-type, spiral null points) are applied to describe the two MR types.

In this section, the MFLs' drastic change and/or the MFLs' breakout-induced self-generating current density fields evolution are simulated and the transformation-transportation between the magnetic energy and plasma current density under two different MR types is investigated.

Fig. 4 depicts the distribution of the current density J in the 4D temporal-spatial scale when the turbulence of the current density enters into the nonlinear stage.

The skeleton fan, spine geometry and topology structure induced by the parallel component of the current density ($J_{\|}$), and the null field line geometry and topology structure induced by the perpendicular component of the current density ($J_{\perp}$) can be seen clearly from Figs. 4–6 [81].

The magnetic tension in the drastic changes of the MFLs gradient sites can be defined as $\frac{(\tilde{\boldsymbol{B}}\cdot\nabla)\tilde{\boldsymbol{B}}}{4\pi}$, then the speed of the wave pulse ($\boldsymbol{V}_w$) traveling along the MFLs can be determined by the plasma inertia force ($nm_i\frac{d\boldsymbol{V}}{dt}$) and the plasma tension. $\boldsymbol{V}_w$ can be defined as follows,

$$V_w = \sqrt{tension/inertia} \tag{16}$$

Eq. (16) shows that the greater the magnetic tension placed on the MFLs, the faster the waves travel. An increase in the magnetic tension will causes an increase in the velocity of the waves traveling on the MFLs. From the turbulence evolution of current density fields at the developing nonlinear stage (67.946 s) and the developed nonlinear stage (74.94 s), the KAW pulse ($\bar{\lambda}_{\perp}$, $\bar{\lambda}_{\|}$, $\tilde{\lambda}_{\perp}$, $\tilde{\lambda}_{\|}$) from the parallel current density ($\bar{\boldsymbol{J}}_{\perp}$, $\bar{\boldsymbol{J}}_{\|}$, $\tilde{\boldsymbol{J}}_{\perp}$, $\tilde{\boldsymbol{J}}_{\|}$) can be seen clearly in Figs. 5 and 6.

The small-scale perturbation of the current density $\tilde{\boldsymbol{J}}(\tilde{\boldsymbol{J}}_{\|}, \tilde{\boldsymbol{J}}_{\perp})$ induced small scale KAW pulses $\tilde{\lambda}(\tilde{\lambda}_{\|}, \tilde{\lambda}_{\perp})$ will perform formation, growth and propagation at the linear, quasilinear and nonlinear turbulence evolution processes.

In the fully developed nonlinear stage, the small-scale KAW pulses will grow up, and some of the small-scale KAW pulses will change to the macro scale KAW pulse $\bar{\lambda}(\bar{\lambda}_{\|}, \bar{\lambda}_{\perp})$.

When we enlarged the macro scale KAW pulses sites, the fine structure of the macro scale KAW pulses also includes several small scale KAW pulses (Figs. 4–6).

Comparing the geometric and topology structure of the turbulence of the current density fields in the nonlinear stage (Fig. 6) and that of the fluctuation of the magnetic fields in the nonlinear stage (Figs. 2 and 3), we can see that the 1st type MR dominates in the developing nonlinear stage. The magnetic tension ($\frac{(\tilde{\boldsymbol{B}}\cdot\nabla)\tilde{\boldsymbol{B}}}{4\pi}$) increases as the value of $\nabla\boldsymbol{B}$ increases, so

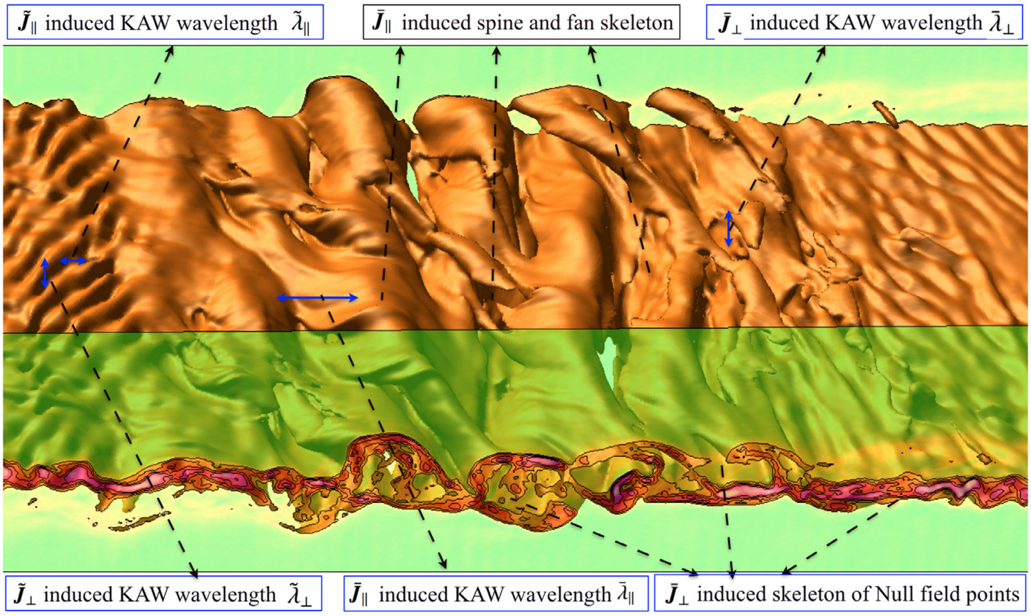

Fig. 5. Topology and evolution of the current density fields at 67.946 s

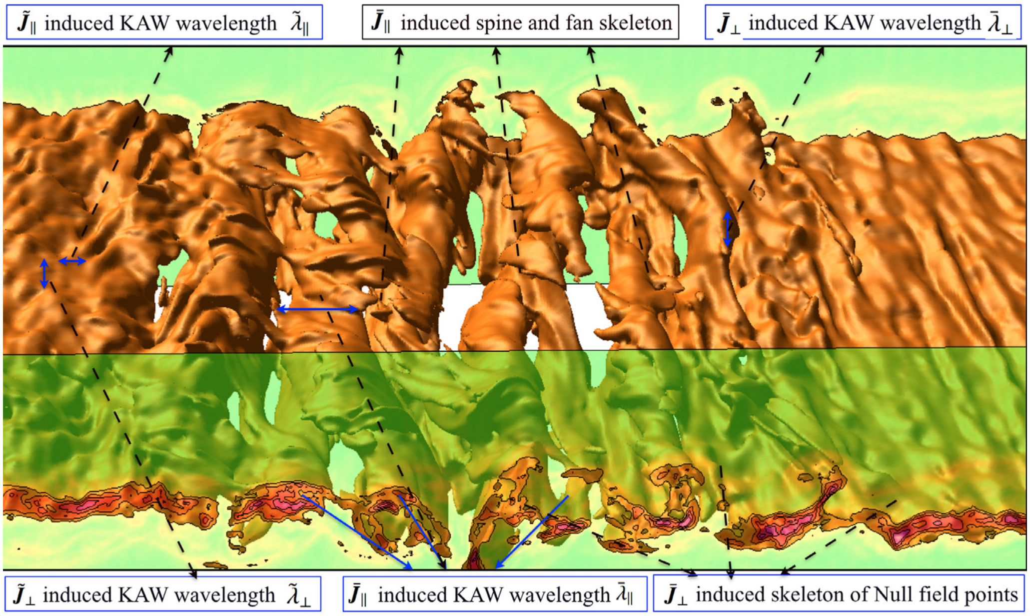

Fig. 6. Topology and evolution of the current density fields at 74.94 s

the MFLs become increasingly "***tighter***" and will reach a maximum limitation and breakout. Then, the 1st type MR changes to the 2nd type MR.

As time goes on, the 2nd type MR become stronger along with the turbulence entering into the fully developed stage. The interaction of KAWs and the charged particle will lead to the magnetic field potential energy translating into the charged particles when the wave number (or pulse) of the KAWs ($k(k_{\parallel}, k_{\perp})$) is larger than that of the charged particles.

Analyzing small scale KAW and macro scale KAW relations during the evolution process (Figs. 4–6) can be helpful for understanding the difference between the MHD Alfvén turbulence (large wavenumber perpendicular to the mean magnetic field) and the Kinetic Alfvén turbulence (different from the MHD Alfvén waves).

Of course, if we also consider the effect of the magnetic pressure on $\nabla \boldsymbol{B}$, the magnetic energy release-conversion in the 1st type MR will become more complex, especially for the low-β case.

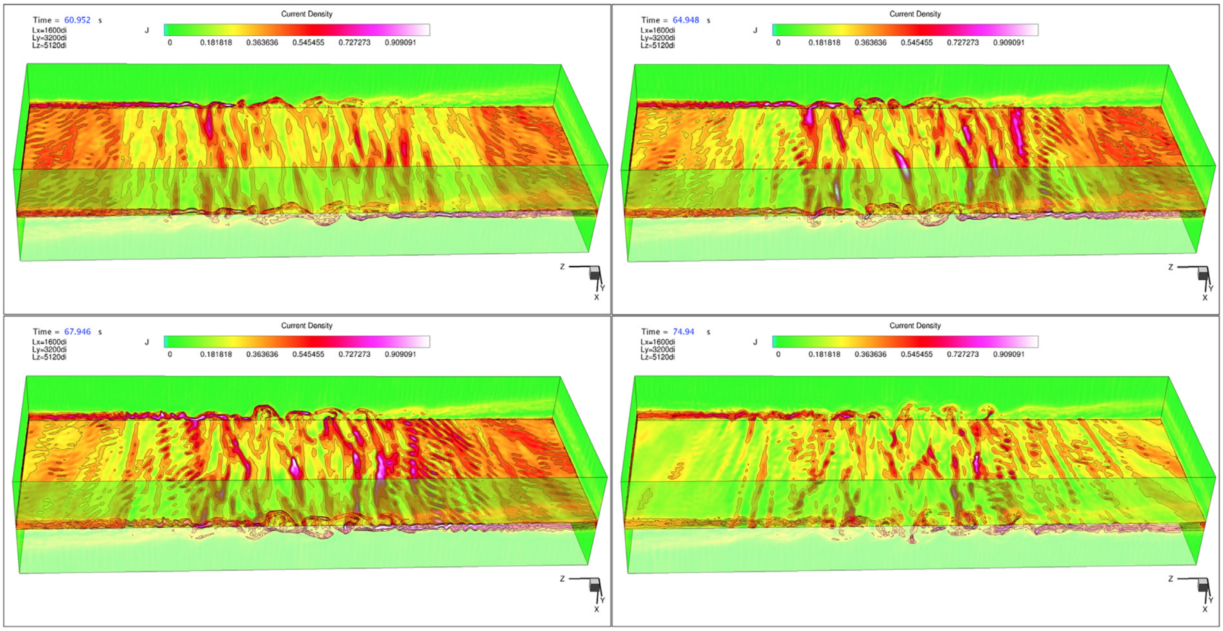

Fig. 7. Current density contour on the cross-section perpendicular to the x axis in the diffusion regions from 60.952 s to 74.94 s

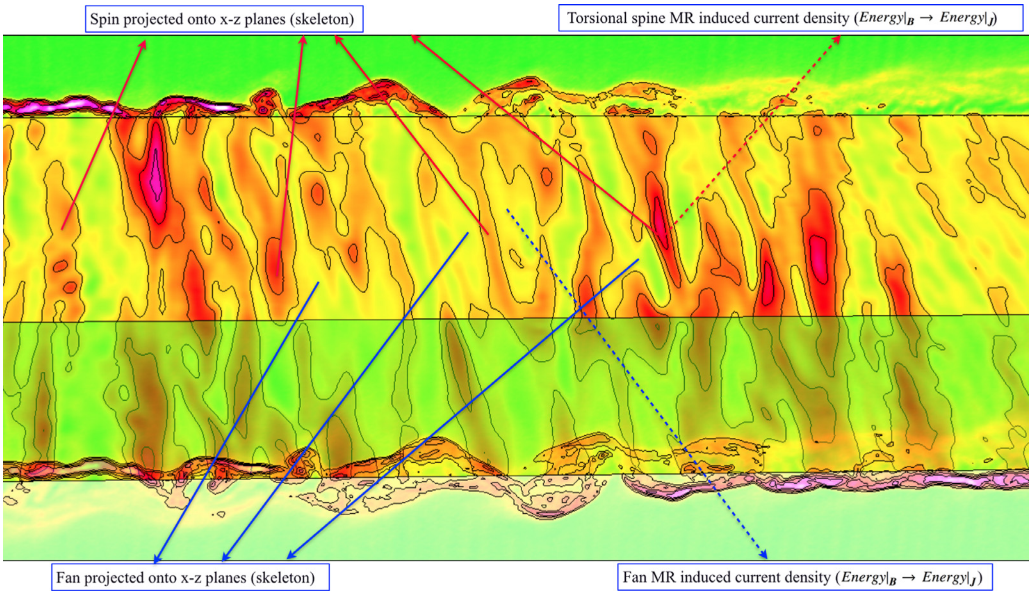

Fig. 8. Current density contour on the cross-section perpendicular to the x axis at 60.952 s

4.2.2. Turbulence of the current density distribution on different cross-sections

The current density distribution on the cross-sections perpendicular to the yz plane and parallel to the 1st type MRs plane are shown in Figs. 7–12, respectively.

From the distribution of the current density contour in the diffusion region at different cross-sections, we can see that the current density values in the spine sites are significantly higher than those in the span sites, which reflects that the role of the 1st type MR in the magnetic energy release-conversion is stronger than the 2nd type MR.

In the linear and quasilinear turbulence stage, the spine is continuous and the increase in the 1st type MRs-induced current density is very significant (Figs. 7–9 and Figs. 10–12, respectively).

On the fully developed nonlinear turbulence stage, the spine structure breaks into many small pieces and the 2nd type MRs become stronger, which is in consistent with the turbulence of the magnetic helical structure analysis in the above sections (Figs. 1–3).

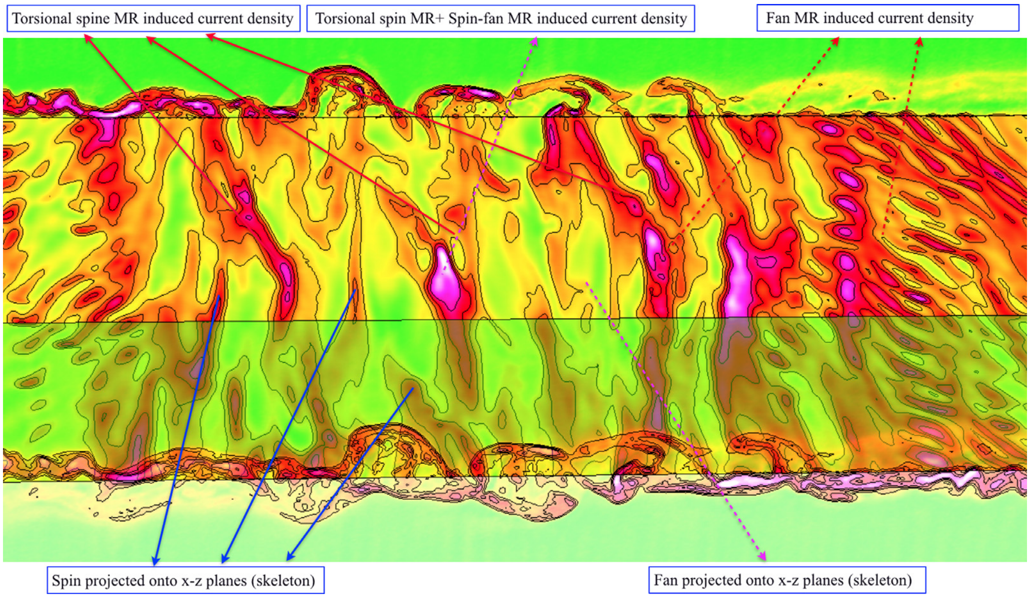

Fig. 9. Current density contour on the cross-section perpendicular to the *x* axis at 67.946 s

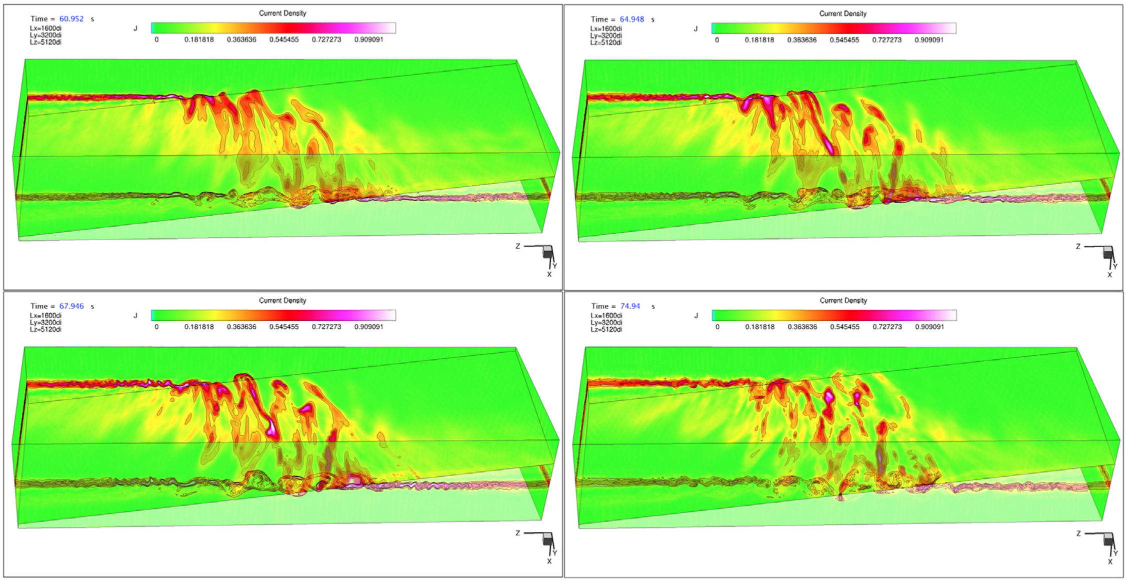

Fig. 10. Current density contour on the cross-section parallel to the slipping MR plane in the diffusion regions from 60.952 s to 74.94 s

From the current density value on the cross-section parallel to the 1st type MR plane (Figs. 10–12), we can also find that the oblique instabilities from a finite fluctuation (component of the fluctuation magnetic fields, component of the turbulence plasmas motion, and the interaction between them) exist in the 1st and 2nd type MRs simultaneously.

In the linear and quasilinear turbulence stages, with the development of the flux rope twist and kink, the oblique instabilities increase and become increasingly obvious. At this stage, the magnetic tension (plus the magnetic pressure) and the MFLs inertia are of the same order, and the QSLs can be clearly seen on the cross section.

On the fully developed nonlinear turbulence stage, the magnetic tension (plus the magnetic pressure) is much higher than the MFLs inertia, and the tearing instabilities become stronger, so both QSLs and SLs can be clearly seen on the cross-section.

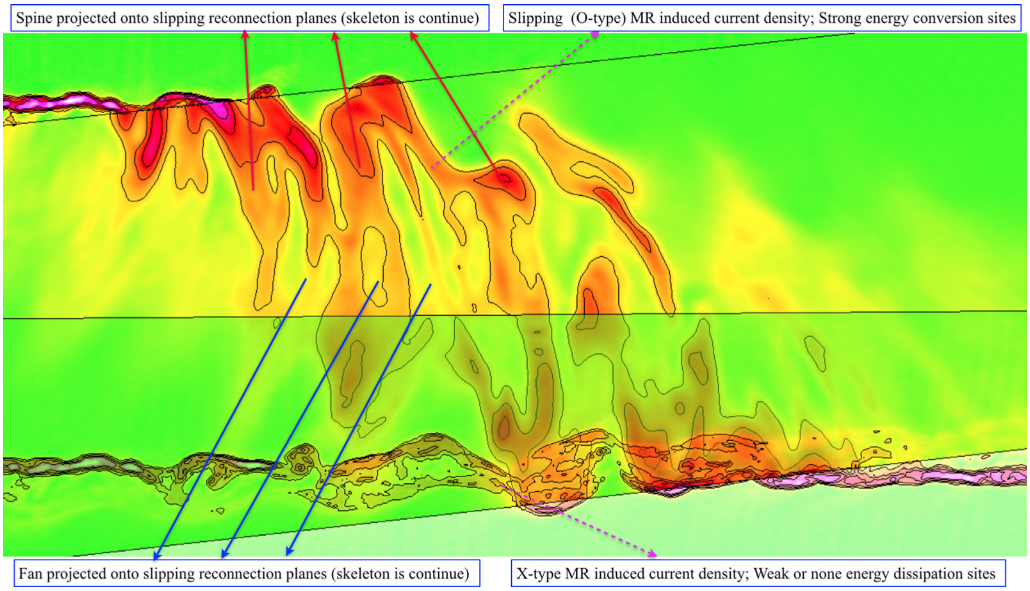

Fig. 11. Current density contour on the cross-section parallel to the slipping MR plane at 60.952 s

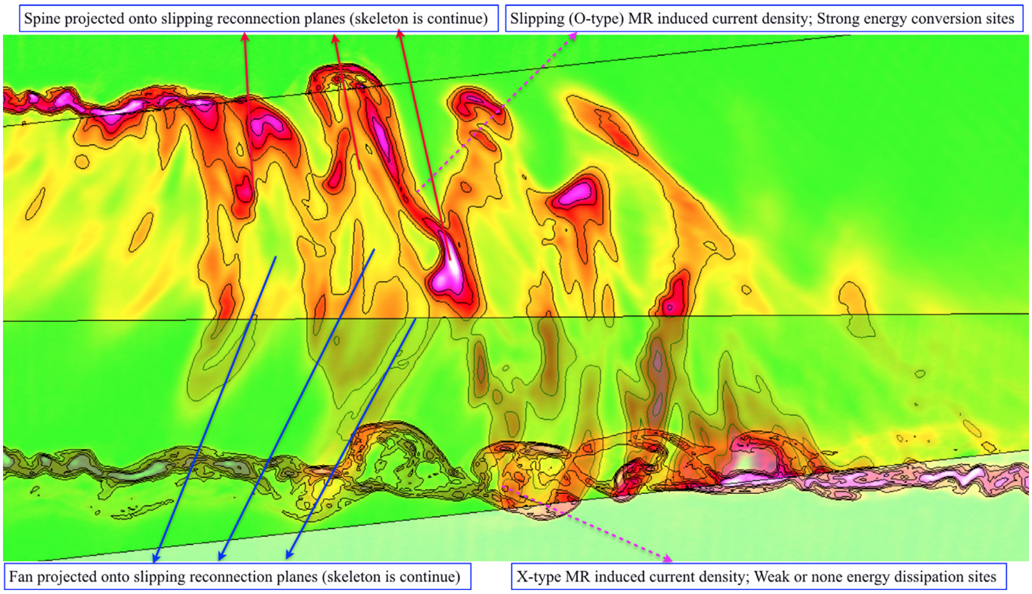

Fig. 12. Current density contour on the cross-section parallel to the slipping MR plane at 67.946 s

4.3. Turbulence of magnetic self-generating-organization and plasma self-feeding-sustaining

Recent research has found that the electrons and ions that decouple (considering the continuous coupled EMHD, HMHD and IMHD process together instead of only considering the IMHD process and neglecting the EMHD-IMHD process) in the diffusion region are the most important aspect for understanding the turbulence mechanism of magnetic field self-generating-organization and plasma self-feeding-sustaining. It can be helpful to explore the LTSTMR from a continuous microphysics (EMHD)-Hall physics (HMHD)-macrophysics (IMHD)-large scale physics (Hydro) coupled scale.

However, the 2D/2.5D MR model does not allow us to investigate the evolution behavior on the cross-section parallel to the CS direction (the 2D/2.5D MR model cannot analyze the turbulence of the magnetic helical structure, the current density vector fields, the self-generating-organization magnetic potential vector fields, the self-feeding-sustaining plasma motion, or the ion and electron acceleration that was created by the perturbation $\nabla \boldsymbol{B}_z$, $\nabla \boldsymbol{U}_z$ in the z direction) and thus eliminates the possible instabilities along the MR line transverse to the MR plane (Oblique instability and Oblique-kink mixed instability), which may result in anomalous diffusion.

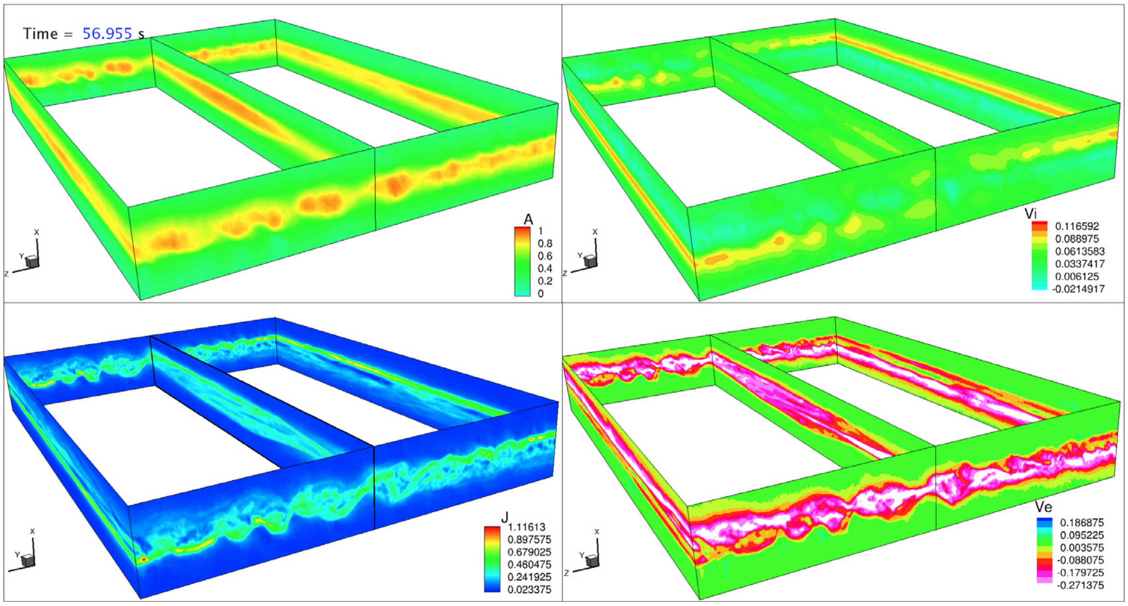

Fig. 13. The magnetic potential, current density, ion velocity and electron velocity evolutions at 56.955 s.

The 2D/2.5D MR model also cannot provide any information on whether the MR is patchy or remains with 2D properties with an extended neutral line when analyzing the natural 3D LTSTMR evolution process (In the natural MR phenomena, all MRs have a three-dimensional case).

In present 3D simulation, the magnetic potential vector ($\boldsymbol{A}$), the current density vector ($\boldsymbol{J}$), the velocity vector of the ion ($\boldsymbol{V}_i$) and electron ($\boldsymbol{V}_e$) evolution process in the continuous temporal-spatial scale are given in Figs. 13–16 and Fig. A.1.

From the simulation evidence, we can see that the current density field is produced by the changing magnetic fields, and the magnitude and direction of the magnetic fields are continuously changing in the temporal-spatial space.

The current density enhancement sites coincide with the magnetic field weakening sites (the current density is stronger, while the magnetic fields are much weaker), which is consistent with $\partial\tilde{\boldsymbol{B}}/\partial t + \nabla\times\tilde{\boldsymbol{E}} = 0$.

The more general self-generating-organization magnetic fields in these sites can be estimated from the growth rate of the magnetic induction. The formula can be written as [82,83],

$$\frac{\partial \boldsymbol{B}}{\partial t} = \nabla\times\boldsymbol{U}\times\boldsymbol{B} - \frac{\nabla\times(\boldsymbol{J}\times\boldsymbol{B})}{nq} - \nabla\times(\eta_{\|}\boldsymbol{J}_{\|} + \eta_{\perp}\boldsymbol{J}_{\perp}) + \frac{\nabla T_e\times\nabla n + \nabla\times\left(0.71n\nabla_{\|}T_e + 1.5n\Omega_e^{-1}\tau_e^{-1}\boldsymbol{b}\times\nabla T_e\right)}{nq} \quad (17)$$

The current density produced from the electromagnetic waves is closely linked with the second and third terms on the right side of the above equation, the third and fourth terms on the right side of the above equation are a source for the self-generated magnetic field.

Thus, the self-magnetic field tends to be generated when the plasma density and temperature gradients are not parallel or when there is a nonzero curl of the thermal force ($\nabla T_e\times\nabla n\neq 0$), which is consistent with previous research [84–87].

Combining the above KAWs analysis and the numerical evidence in this section, we can also see that the initial fluctuation of the magnetic field ($\tilde{\boldsymbol{B}}$) and the fluctuation component of the KAWs energy tend to increase the gradients of the plasma's density and temperature.

The skeleton of the magnetic potential field and the current density field have similar geometry and topology structures in the same *xz* and *xy* cross sections, which illustrates that the magnetic field self-generating-organization, plasma self-feeding-sustaining occurs at the same time and location, and these evolutions belong to the mixed type MR (1st type and 2nd type) evolution.

The interaction of the magnetic field KAWs-to-magnetic field KAWs, magnetic field KAWs-to-plasma KAWs, plasma KAWs-to-plasma KAWs, magnetic field KAWs-to-charged particles, and plasma KAWs-to-charged particles will accelerate the ion and electron particles during the energy transportation process between the magnetic field and the plasma around *O*-type and *X*-type null points.

Since the mass of the ion is much larger than that of the electron, the velocity of the electron is much larger than that of the ion during the linear turbulence evolution stage (Fig. 13). As the time goes on, the electron will reach the maximum velocity bin first, while the ion will still stay in a relatively low velocity bin in the linear-to-nonlinear LTSTMR evolution stage (Fig. 14).

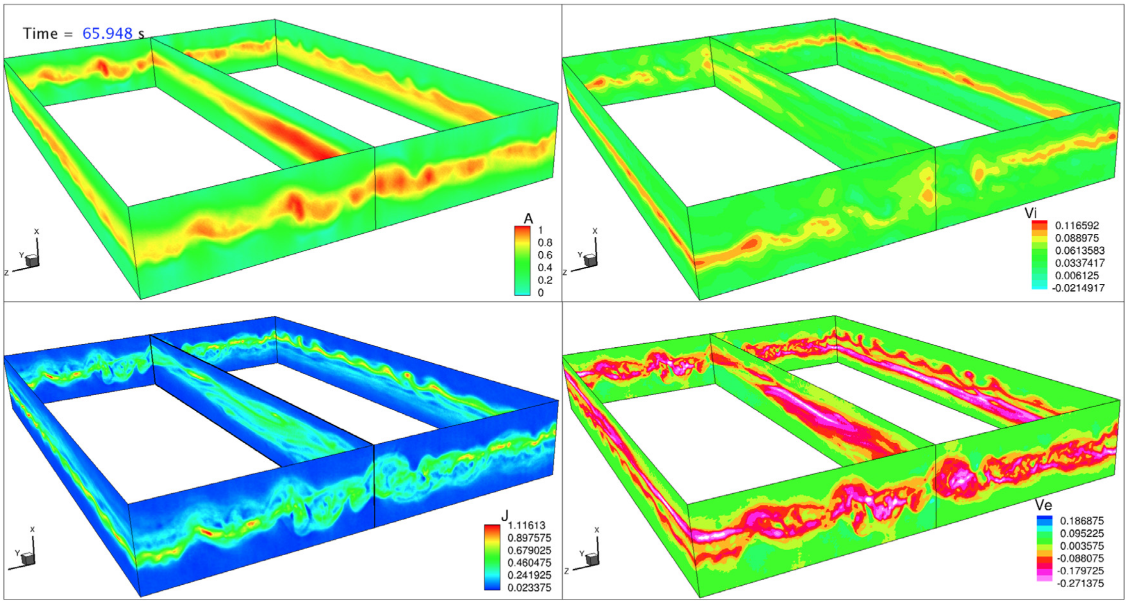

Fig. 14. The magnetic potential, current density, ion velocity and electron velocity evolutions at 65.948 *s*.

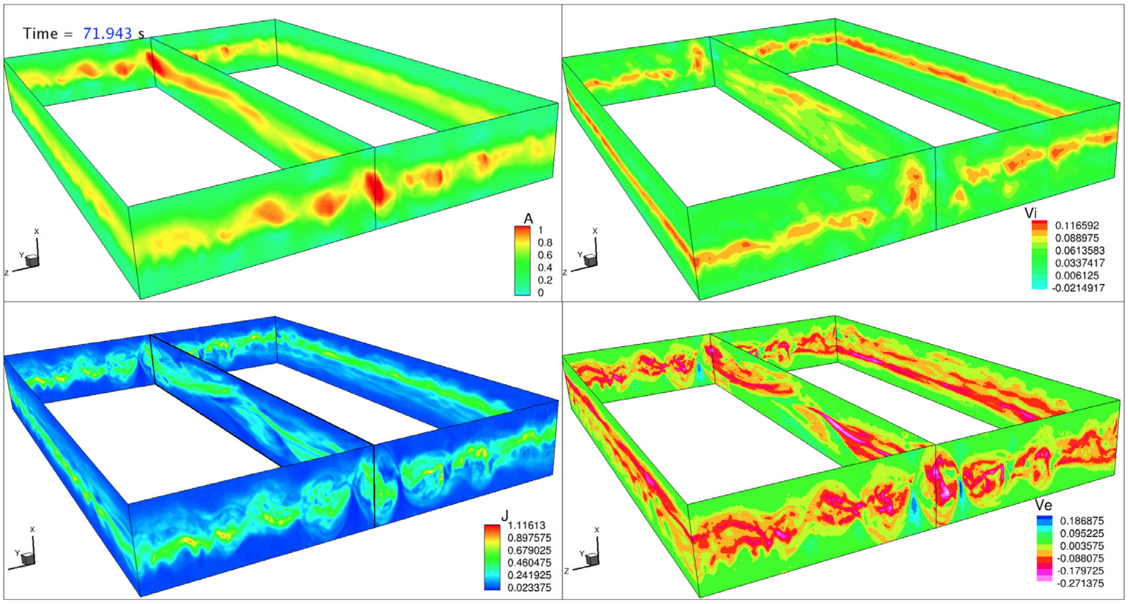

Fig. 15. The magnetic potential, current density, ion velocity and electron velocity evolutions at 71.94 s.

As the evolution enters into the fully developed nonlinear stage, both the ion and electron reach their maximum velocity bin. The ion has a higher energy level ($\sim$ GeV) than the electron ($\sim$ MeV) (Figs. 15 and 16), which agrees with observations [24–27,74–76].

We can also see that the electron acceleration sites are obviously much larger than the ion acceleration sites, and the ion acceleration sites only appear in the center of the spine zone (interior of the magnetic islands/flux ropes), while the electron acceleration appears both in the spine and fan zone (inertia and boundary of the magnetic islands/flux ropes). In the same position, the velocity direction of the ion and electron are opposite.

For the self-feeding-sustaining plasma turbulence in the diffusion region, the evolution from the linear stage to the fully developed nonlinear stage can be clearly seen during the velocity evolution of the charged particle, which also agrees with previous research [77–79].

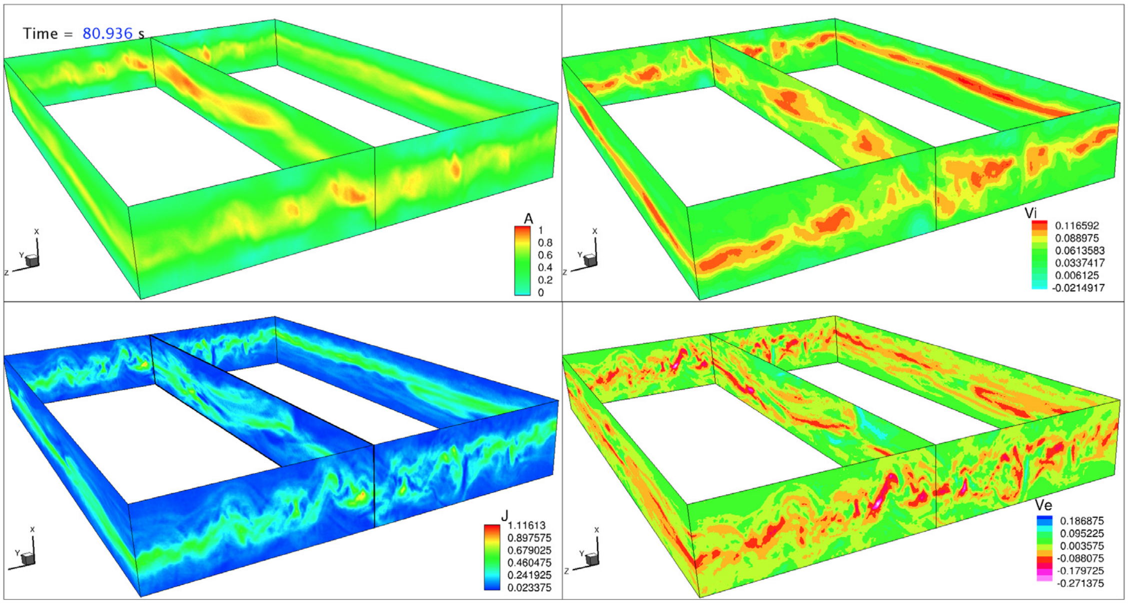

Fig. 16. The magnetic potential, current density, ion velocity and electron velocity evolutions at 80.396 s.

The formation-merging-coalescent of the plasma bubbles (vortex that is induced from the perturbation of the plasma velocity $\tilde{\boldsymbol{U}}$, magnetic strength $\tilde{\boldsymbol{B}}$, and the interaction between $\tilde{\boldsymbol{U}}$, and $\tilde{\boldsymbol{B}}$,) can occur in both small-scale and macroscale KAW time in the continuous kinetic-dynamic-hydro temporal-spatial evolutions process, which leads the localized MR self-feeding-sustaining sites to appear and grow in the diffusion region, until it is full of the entire resistive domain.

This manner of self-feeding-sustaining can also explain why MR occurs and develops much faster at the EMHD-HMHD scale than at the IMHD-large hydroscale, which also give rise to the fact that the MR rate calculated with the EMHD-HMHD-IMHD MR model is much larger than the value calculated with the IMHD-large hydro scale MR model.

4.4. Turbulence acceleration mechanism

For a charged particle's turbulence acceleration mechanism in the diffusion region of the LTSTMR, the original 2D/2.5D MR model cannot determine it due to the lack of analyzing the interaction of the flux rope, especially in the vicinity of multi-flux ropes (flux rope networks and sub flux ropes, 1st type MR). Then, the role of the turbulence acceleration mechanism in the coupling kinetic-dynamic-hydro LTSTMR process remains an open question.

Some researchers prefer to believe that the turbulence acceleration mechanism depends on the Fermi acceleration mechanism, while some others prefer to believe that the turbulence acceleration mechanism is an independent acceleration mechanism.

In solar physics, most researchers prefer to define the turbulence acceleration mechanism as a plasma turbulent acceleration mechanism, formed by the plasma's motion fluctuation components-induced waves, which are propagation and amplified through waves-to-waves interactions and waves-to-particles interactions. It is an independent turbulent acceleration mechanism, but until now there has been no evidence from simulations that can verify the phenomena in 3D MR [12–16,23–27].

In this section, the particle acceleration path-line of a mixed MR (1st type and 2nd type) in the diffusion region around the O and X null points is investigated (Fig. 17, Supplementary videos 6–9).

From the above KAW discussion, we can see that the interaction of $\tilde{\boldsymbol{B}}$-to-$\tilde{\boldsymbol{J}}$ KAWs and $\tilde{\boldsymbol{U}}$ KAWs-to-charged particle velocity provide the possibility of turbulence acceleration (Supplementary video 5).

The waves-to-waves ($\lambda_{\tilde{\boldsymbol{B}}} - to - \lambda_{\tilde{\boldsymbol{U}}}$, $\lambda_{\tilde{\boldsymbol{J}}} - to - \lambda_{\tilde{\boldsymbol{U}}}$) interactions and the waves-to-particles ($\lambda_{\tilde{\boldsymbol{B}}} - to - \lambda_{\boldsymbol{V}}$, $\lambda_{\tilde{\boldsymbol{J}}} - to - \lambda_{\boldsymbol{V}}$, $\lambda_{\tilde{\boldsymbol{U}}} - to - \lambda_{\boldsymbol{V}}$) interactions will accelerate the charged particles in the turbulence of a magnetic self-generating-organization (magnetic fields' fluctuation caused by acceleration, $\tilde{\boldsymbol{B}}$) and plasma self-feeding-sustaining (plasma turbulence caused by acceleration, $\tilde{\boldsymbol{U}}$) evolution process, which verifies that the source of the turbulence acceleration mechanism is the resonance effect of the waves (fluctuation of the magnetic field, turbulence of the current density field, and turbulence of the plasma velocity field) and the charged particle velocity.

The turbulence acceleration mechanism is different from the Fermi (or shock wave) acceleration mechanism, which is an independent acceleration mechanism as well as an original hybrid acceleration mechanism (composed of parallel electric fields, betatrons, shock and Fermi).

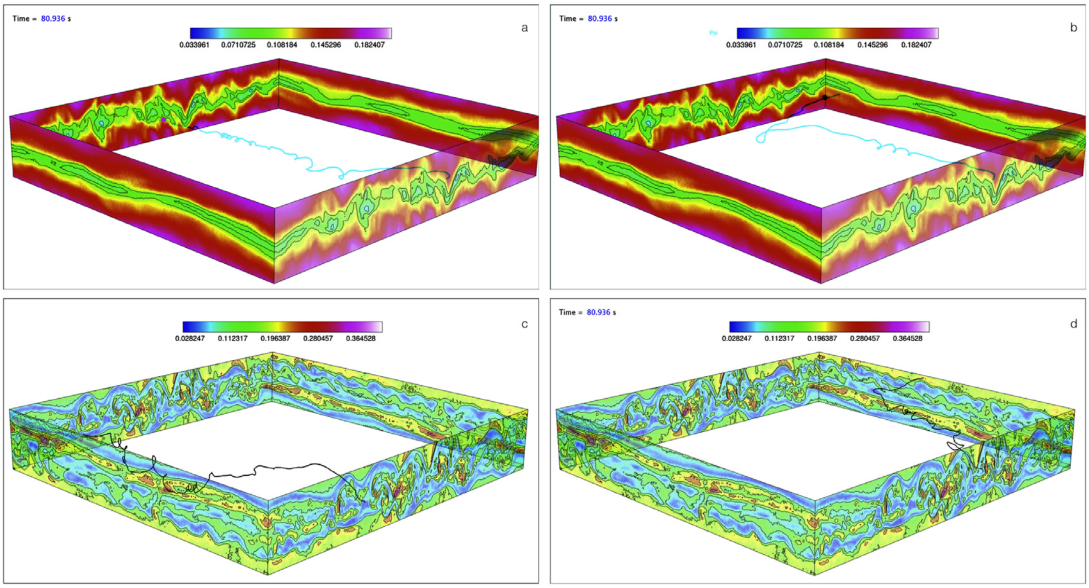

Fig. 17. Ion and electron particle acceleration path-line from 42.966 s–80.936 s. (Supplementary videos 6–9)

Comparing the trajectories of the particles in 3D (Fig. 17 and Supplementary videos 6–9) and in 2D/2.5D (Supplementary video 10) temporal-spatial scales, we can see that the spiral path line (formed in the mixed *O* and *X* type MR) appears in the ion and electron acceleration processes, which is consistent with the previous mixed instabilities (mixed oblique-kink-tearing instabilities) and mixed MR (1^{st} and 2nd type MR) analysis in the above sections.

Comparing the 3D trajectory (Fig. 17 and Supplementary videos 6–9) with the RHPIC-LBM 2.5D adjacent magnetic islands (Supplementary videos 3–4) coalescence process [80], we can also verify and confirm that the slipping MR-induced acceleration mechanism domainates in the continuous kinetic-dynamic-hydro fully coupled evolution process.

5. Summary and concluding remarks

The two parts focus, in turn, on (i) the RHPIC-LBM model, algorithm and code development and verification, and (ii) its application in the 3D LTSTMR.

In this paper, the role of turbulence in the flux rope interaction is investigated with RHPIC-LBM through simulations on 100,000 CPU cores of the ***Tianhe-2*** at the NSCC-GZ super computer platform. The magnetic energy release-conversion, plasma heating, charged particles energization and acceleration in the self-generating-organization magnetic field region and self-feeding-sustaining diffusion plasma region are obtained. A summary of the main points is given below:

(i) Slipping MR exists in the adjacent MFLs compress-stretch-slip process on the QSLs (a drastic change in the MFL linkage span) and adjacent MFLs break-rejoin MR exists on the SLs, which agrees with observation [19,20].

(ii) The slipping MRs and the MFLs' break-rejoin MRs are closely linked with oblique instabilities and resistive tearing instabilities, respectively. The 1st type MR forms *O*-type null points, and the 2nd type MR forms *X*-type null points. The magnetic energy conversion is dominated by turbulence-induced oblique instabilities (*O*-type) in the 3D model instead of resistive tearing instabilities (*X*-type) in the 2D/2.5D model, which are well consistent with 3D observations [21–23]. iii) The magnetic energy conversion is produced during the interaction of the plasmoid-to-flux rope, plasmoid-to-plasmoid, and flux rope-to-flux rope. The turbulent acceleration is an independent acceleration mechanism in LTSTMR, induced by the interaction of waves-to-waves and waves-to-particles, which is different from the original hybrid acceleration mechanism (composed of parallel electric fields, betatrons, shock and Fermi).

(iv) The particles can be energized and accelerated in a longer time scale ($\sim$30 s) and can be accelerated to relativistic energies ([74–76]) after being pre-accelerated by Fermi-Betatron-shock wave acceleration. These are in agreement with observations [24–27].

Conflict of interest

No.

Acknowledgments

This work was supported by the strategic priority research program of CAS (XDA17040507, XDA15010900), the national basic research program of China (2013CBA01503), the key program of NSFC (11333007), joint funds of NSFC (U1631130), frontier science key programs of CAS (QYZDJ-SSWSLH012), the program for innovation team of Yunnan Province, the program for Guangdong introducing Innovative and entrepreneurial teams (2016ZT06D211), and the special program for applied research on super computation of the NSFC-Guangdong joint fund (second phase) under No. U1501501. We thank the editors and the anonymous reviewers for their comments that greatly improved the manuscript. Thanks to Prof.Y.L.Shi of University of Chinese Academy of Sciences for helpful discussion on LBM parts. Thanks Prof.Y.T.Lu, Dr. W.Wan, Dr. H.Z.Lu and other members of NSCC-GZ for super computer services. Thanks to Dr.L.P.Liu, Prof.X.B.Chi and other members of computer network information center of CAS for HPC services. Thanks to Dr. Hui Li, Dr. Shengtai Li, Dr. Fan Guo, Dr. Xiaocan Li and other members of T2 and T5 Division of Los Alamos National Laboratory for helpful discussion on vortex/turbulence role on particles accelerations and magnetic energy translation. Thanks to Dr. Y. Li and Prof. J. Lin of Yunnan Observatories of CAS for helpful discussion on particle acceleration and solar physics. Thanks to Dr.W.Jin of Kunming Radio Wave Observatory of CRIRP for helpful discussion on observations of space physics.

Appendix

Supplementary documents

Supplementary video 1: 3D structure and evolution of a single magnetic turbulence seed from RHPIC-LBM.
https://pan.cstcloud.cn/s/6jy6QYQYRew
Supplementary video 2: Magnetic structure and evolution in the 3D magnetic reconnection from RHPIC-LBM.
https://pan.cstcloud.cn/s/8CfcC02IS2I
Supplementary video 3: The coalescence process of two adjacent magnetic islands.
http://ddl.escience.cn/f/QSWa
Supplementary video 4: The coalescence process of three adjacent magnetic islands.
http://ddl.escience.cn/f/QSWB
Supplementary video 5: The coalescence of two adjacent magnetic islands before ejection.
https://pan.cstcloud.cn/s/AQzJ5FC3TLs
Supplementary video 6: Selected ion particle A animation file for tracking trajectories in temporal-spatial space from 3D RHPIC-LBM.
http://ddl.escience.cn/f/QJzL

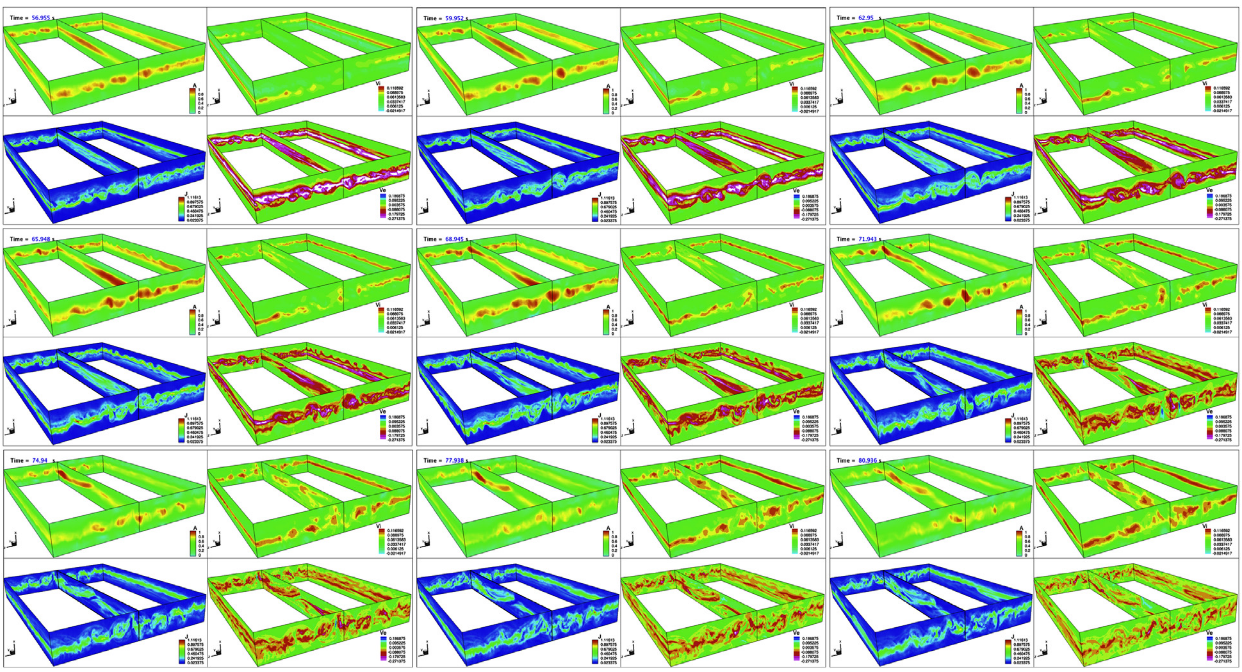

Fig. A.1. The magnetic potential vector, current density, ion velocity and electron velocity evolution during 56.955 s–80.936 s.

Supplementary video 7: Selected ion particle B animation file for tracking trajectories in temporal-spatial space from 3D RHPIC-LBM.

http://ddl.escience.cn/f/QJzM

Supplementary video 8: Selected electron particle C animation file for tracking trajectories in temporal-spatial space from 3D RHPIC-LBM.

http://ddl.escience.cn/f/QJzN

Supplementary video 9: Selected electron particle D animation file for tracking trajectories in temporal-spatial space from 3D RHPIC-LBM.

http://ddl.escience.cn/f/QJzO

Supplementary video 10: Selected particles animation file for tracking trajectories in temporal-spatial space from 2.5D RHPIC-LBM.

http://ddl.escience.cn/f/QJA5

References

[1] H.T. Ji, W. Daughton, Phase diagram for magnetic reconnection in heliophysical, astrophysical and laboratory plasmas, Instrum. Meth. Astrophys. 18 (2011) 111207.
[2] P.A. Cassak, J.F. Drake, On phase diagrams of magnetic reconnection, Phys. Plasmas. 20 (2013) 061207.
[3] H.R. Yan, Cosmic ray transport in turbulent magnetic field. magnetic fields in diffuse media, in: Astrophysics and Space Science Library, 407, Springer-Verlag Berlin Heidelberg, 2015, pp. 253–281.
[4] V.N. Tsytovich, Theory of Turbulent Plasma, Springer-Verlag Berlin Heidelberg, 1977.
[5] D. Biskamp, Magnetohydrodynamic Turbulence, Cambridge University Press, 2003.
[6] J. Chen, Physics of erupting solar flux ropes: coronal mass ejections (CMEs)-recent advances in theory and observation, Phys. Plasmas. 24 (2017) 090501.
[7] M. Takamoto, A. Lazarian, Strong coupling of alfvén and fast modes in compressible relativistic magnetohydrodynamic turbulence in magnetically dominated plasmas, Mon. Notices Royal Astron. Soc. 472 (4) (2017) 4542–4550.
[8] S.Y. Xu, A. Lazarian, B. Zhang, The generation, destination, and astrophysical applications of magnetohydrodynamic turbulenceł, AAS Meet. 229 (2017). 435.04
[9] M.A. Shay, C. Haggerty, T. Parashar, W. Matthaeus, R. Bandyopadyay, T.D. Phan, J.F. Drake, Y. Yang, M. Wan, S. Servidio, Statistics of magnetic reconnection in turbulence and its effect on plasma heating, SHINE. 2018 (2018) 34.
[10] J.C. Meyer, Structure of the Diffusion Region in Three Dimensional Magnetic Reconnection, University of Delaware, 2015. Ph.D Dissertation
[11] M.R. Brownb, D.A. Schaffner, P.J. Weck, Magnetohydrodynamic turbulence: observation and experiment, Phys. Plasmas. 22 (2015) 055601.
[12] D.I. Pontin, Three-dimensional magnetic reconnection regimes: a review, Adv. Space. Res. 47 (9) (2011) 1508–1522.
[13] B. Ripperda, O. Porth, C. Xia, R. Kepens, Reconnection and particle acceleration in interacting flux ropes -II. 3d effects on test particles in magnetically dominated plasmas, Mon. Notices. Royal. Astron. Soc. 471 (3) (2017) 3465–3482.
[14] P. Zhu, A. Bhattacharjee, A. Sangari, Z. Wang, P. Bonofiglo, Three-dimensional geometry of magnetic reconnection induced by ballooning instability in a generalized harris sheet, Phys. Plasmas. 24 (2) (2017) 024503.
[15] Z. Akbari, M. Hosseinpour, M.A. Mohammadi, Particle acceleration in three-dimensional reconnection of flux-tube disconnection, Astrophys. Space. Sci. 361 (11) (2016) 355.
[16] E. Priest, MHD structures in three-dimensional reconnection, Astrophys. Space Sci. Libr. (2016) 101–142.
[17] J.J. Drake, J.M. Laming, K.G. Widing, H.H. Jurgen, B. Haisch, S. Bowyer, The elemental composition of the corona of procyon: Evidence for the absence of the FIP effect, Science. 267 (5203) (1995) 1470–1473.
[18] K.J. Phillips, Abundances in the solar corona, Adv. Space. Res. 20 (1997) 79.
[19] T.Y. Gou, R. Liu, Y.M. Wang, K. Liu, B. Zhang, J. Chen, Q.H. Zhang, J.J. Liu, Stereoscopic observation of slipping reconnection in a double candle-flame-shaped solar flare, Astrophys. J. Lett. 821 (2) (2016) L28.
[20] Y. Chen, G.H. Du, D. Zhao, Z. Wu, W. Liu, B. Wang, G.P. Ruan, S.W. Feng, H.Q. Song, Imaging a magnetic-breakout solar eruption, Astrophys. J. Lett. 820 (2) (2016) L30.
[21] H.S. Fu, A. Vaivads, Y.V. Khotyaintsev, M. Andre, J.B. Cao, V. Olshevsky, J.P. Eastwood, A. Retino, Intermittent energy dissipation by turbulent reconnection, Geophys. Res. Lett. 44 (1) (2016) 37–43.
[22] M. Zastrow, For magnetic reconnection energy, O-not X-might Mark Spot, EOS 98 (2017).
[23] W.Q. Gan, D.Y. Wang, Solar high-energy physics, CSPM, Bei Jing, (2016) 1–317.
[24] N.B. Crosby, M.J. Aschwanden, B.R. Dennis, Frequency distributions and correlations of solar x-ray flare parameters, Sol. Phys. 143 (2) (1993) 275–299.
[25] R.P. Liu, B.R. Dennis, G.J. Hurford, D.M. Smith, A. Zehnder, P.R. Harvey, D.W. Curtis, D. Pankow, P. Turin, M. Bester, A. Csillaghy, M. Lewis, N. Madden, H.F. Van beek, M. Appleby, T. Raudorf, J. Mctiernan, R. Ramaty, E. Schmahl, R. Schwartz, S. Krucker, R. Abiad, T. Quinn, P. Berg, M. Hashii, R. Sterling, R. Jackson, R. Pratt, R.D. Campbell, D. Malone, D. Landis, C.P. Barrington-leigh, S.S. Senn, C. Cork, D. Clark, D. Amato, L. Orwig, R. Boyle, I.S. Banks, K. Shirey, A.K. Tolbert, D. Zarro, F. Snow, K. Thomsen, R. Henneck, A. Mchedlishvili, P. Ming, M. Fivian, J. Jordan, R. Wanner, J. Crubb, J. Preble, M. Matranga, A. Benz, H. Hudson, R.C. Ccanfield, G.D. Holman, C. Crannell, T. Kosugi, A.G. Emsile, N. Vilmer, J.C. Brown, C. J. Krull, M. Aschwanden, T. Metcalf, A. Conway, The reuven ramaty high-energy solar spectroscopic imager (RHESSI), Sol. Phys. 210 (1-2) (2002) 3–32.
[26] G.A. Dulk, A.L. Kiplinger, R.M. Winglee, Characteristics of hard x-ray spectra of impulsive solar flares, Astrophys. J. 389 (1992) 756–763.
[27] P. Eger, Identification of Tev-ray sources through multi-wavelength studies, Dissertation of Der Naturwissenschaftlichen Fakultat der Friedrich-Alexander-Universitat Erlangen-Nurnberg, 2011, pp. 1–159.
[28] F. Mohseni, Lattice boltzmann models for relativistic hydrodynamics and magnetohydrodynamics, 2015, Ph.D dissertation of ETH Zurich, 1–153
[29] G. Breyiannis, D. Valougeorgis, Lattice kinetic simulations of 3-D MHD turbulence, Comput. Fluids. 35 (2006) 920–924.
[30] M. Mendoza, B.M. Boghosian, H.J. Herrmann, S. Succi, Fast lattice Boltzmann solver for relativistic hydrodynamics, Phys. Rev. Lett. 105 (2010) 014502.
[31] F. Mohseni, M. Mendoza, S. Succi, H.J. Herrmann, Lattice Boltzmann model for resistive relativistic magnetohydrodynamics, Phys. Rev. E. 92 (2015) 023309.
[32] T.K. Nakamura, R. Nakamura, Y. Nartia, W. Baumjohann, W. Daughton, Multi-scale structures of turbulent magnetic reconnection, Phys. Plasmas. 23 (2016) 052116.
[33] J. Neeraj, V.S. Adrian, M. Patricio, B. Jing, G. Olaf, K. Thomas, Electron-magnetohydrodynamic simulations of electron scale current sheet dynamics in the vineta. II guide field reconnection experiment, Phys. Plasmas. 24 (9) (2017) 092312.
[34] L. Franci, S. Landi, A. Verdini, L. Matteini, P. Hellinger, Solar wind turbulent cascade from MHD to sub-ion scales: Large-size 3d hybrid particle-in-cell simulations, Astrophys. J. 853 (1) (2018).
[35] L. Franci, P. Hellinger, M. Guarrasi, C.H.K. Chen, E. Papini, A. Verdini, L. Matteini, S. Landi, Three-dimensional simulations of solar wind turbulence with the hybrid code CAMELIA, J. Phys. Conf. Ser. 1031 (1) (2017).
[36] C. Palenzuela, L. Lehner, O. Reula, L. Rezzolla, Beyond idea MHD: towards a more realistic modelling of relativistic astrophysical plasmas, Mon. Notices Royal Astron. Soc. 394 (4) (2009) 1727–1740.

[37] N. Jain, Study of Electron-Magnetohydrodynamic (EMHD) Phenomena in Plasmas, Gujarat University, 2006. Ph.D Dissertation
[38] D. Biskamp, H. Welter, Coalescence of magnetic islands, Phys. Rev. Lett. 44 (1980) 1069.
[39] A. Bhattacharjee, Y. Yuan, Self-consistency constraints on the dynamo mechanism, Astrophys. J. 449 (1995) 739–744.
[40] M.G. Haines, Magnetic-field generation in laser fusion and hot-electron transport, Can. J. Phys. 64 (8) (1986) 912–919.
[41] E.M. Epperlein, Studies on Collisional Electromagnetic Instabilities and Linear Transport in Laser-Plasmas, Imperial College, 1984. Ph.D Dissertation
[42] E.M. Epperlein, M.G. Haines, Plasma transport coefficients in a magnetic field by direct numerical solution of the Fokker-planck equation, Phys. Fluids. 29 (1986) 1029.
[43] D. Biskamp, Magnetic reconnection in plasmas, in: Cambridge Monographs on Plasma Physics, 3, Cambridge University Press, London., 2000, p. 0521582881.
[44] Y.H. Liu, G.W. Yan, A lattice Boltzmann model for Maxwell's equations, Appl. Math. Model. 38 (2014) 1710–1728.
[45] F. Mohseni, M. Mendoza, S. Succi, H.J. Herrmann, Lattice Boltzmann model for resistive relativistic magnetohydrodynamics, Phys. Rev. E. 92 (2) (2015) 023309.
[46] F. Mohseni, Lattice Boltzmann Models for Relativistic Hydrodynamics and Magnetohydrodynamics, ETH Zurich., 2015, pp. 1–153. Ph.D Dissertation
[47] M. Mendoza, J.D. Muaoz, Three-dimensional lattice Boltzmann model for magnetic reconnection, Phys. Rev. E. 77 (2) (2008) 026713.
[48] M.M. jimenez, B.M. Boghosian, H.J. Herrmann, S. Succi, Fast lattice Boltzmann solver for relativistic hydrodynamics, Phys. Rev. Lett. 105 (2010) 014502.
[49] M.M. Jimenez, Relativistic Fluid Dynamics in Complex Systems, ETH Zurich, 2012. Ph.D Dissertation
[50] J. Bacechner, J.P. Kuska, Sausage mode instability of thin current sheets as a cause of Magnetospheric substorms, Ann. Geophys-Germany. 17 (5) (1999) 604–612.
[51] J. Bacechner, J.P. Kuska, Three-dimensional collisionless reconnection through thin current sheets - theory and self-consistent simulations, ICS-3. (1996) 373–380.
[52] E.G. Harris, On a plasma sheath separating regions of oppositely directed magnetic field, Nuovo. Cimento. 22 (1) (1962) 115–121.
[53] J. Neeraj, J. Bacechner, Three dimensional instabilities of an electron scale current sheet in collisionless magnetic reconnection, Phys. Plasmas. 21 (6) (2014) 62116.
[54] D.N. Walker, J.H. Bowles, W.E. Amatucci, D.L. Holland, J. Chen, The harris magnetic field: a laboratory realization of the topology based on energy resonance, J. Geophys. Res. 109 (2004) A06205.
[55] D.N. Baker, T.I. Pulkkinen, V. Angelopoulos, W. Baumjohann, R.L. McPherron, Neutral line model of substorms: Past results and present view, J. Geophys. Res. Space. Phys. 101 (12) (2006) 12975–13010.
[56] W. Daughton, J. Scudder, H. Karimabadi, Fully kinetic simulations of undriven magnetic reconnection with open boundary conditions, Phys. Plasmas. 13 (2006) 072101.
[57] C.J. Schrijver, Driving major flares and eruptions a review, Adv. Space. Res. 43 (5) (2009) 739–755.
[58] T.G. Forbes, Magnetic reconnection in solar flare, Geophys. Astro. Fluid. 62 (1-4) (1991) 15–36.
[59] V. Archontis, Magnetic flux emergence in the sun, J. Geophys. Res. 113 (2008) A03S04.
[60] V. Archontis, A.W. Hood, Magnetic flux emergence: a precursor of solar plasma expulsion, Astron. Astrophys. 537 (A62) (2012) 1–19.
[61] D. L. Shelton, The Effect of Flux Emergence From the Solar Surface to The Corona, University College London, Thesis, 1–91,2014,
[62] P. Demoulin, J.C. Henoux, E.R. Priest, C.H. Mandrini, Quasi-separatrix layers in solar flare, Astrono. Astrophys 308 (1996) 643–655.
[63] E. Lawrence, W. Gekelman, Identification of a quasiseparatrix layer in a reconnecting laboratory magnetoplasma, Phys. Rev. Lett. 103 (10) (2009) 105002.
[64] W. Gekelman, E. Lawrence, A. Collette, S. Vincena, B.V. Compernolle, P. Pribyl, M. Berger, J. Campbell, Magnetic field line reconnection in the current systems of flux ropes and Alfven waves, Phys. Scripta. 2010 (2010) T142.
[65] M. Hesse, K. Schindler, A theoretical foundation of general magnetic reconnection, J. Geophys. Res. 93 (1988) 5559–5567.
[66] B. Schmieder, C.H. Mandrini, P.D. Demoulin, What is the role of magnetic null points in large flares, Adv. Space. Res. 39 (2007) 1840–1846.
[67] K. Galsgaard, Dynamical investigation of three-diemensional reconnection in quasi-separatrix layers in a boundary-driven magnetic field, J. Geophys. Res. 105 (2000) 5119–5134.
[68] F. Effenberger, J.D. Craig, Simulaition of 3d magnetic merging: resistive scalings for null point and QSL reconnection, Solar. Phys. 291 (2016) 143–153.
[69] G. Aulanier, E. Pariat, P. Demoulin, Slip-running reconnection in QSLs, Solar. Phys. 238 (2006) 347–376.
[70] E. Pariat, G. Aulanier, P.A. Demoulin, A new concept for magnetic reconnection: slip-running reconnection, SF2A. (2006) 559–562.
[71] P. Demoulin, Where efficient energy release occur in 3-d magnetic configurations, Adv. Space. Res. 39 (2007) 1367–1377.
[72] J. Dudik, M. Janvier, G. Aulanier, G.Z. Del, M. Karlicky, E.H. Mason, B. Schmieder, Slipping magnetic reconnection during an x-class solar flare observed by SDO/AIA, Astrophys. J. 784 (2014) 144–165.
[73] M. Janvier, G. Aulanier, From coronal observations to MHD simulations, the building blocks for 3d models of solar flares, Solar Stellar Flare. 290 (12) (2015) 3425–3456.
[74] B. Ripperda, O. Porth, C. Xia, R. Keppens, Reconnection and particle acceleration in interacting flux ropes-i. magnetohydrodynam- ICS and test particles in 2.5D, Mon. Notices. Royal. Astron. Soc. 467 (2017) 3279–3298.
[75] B. Ripperda, O. Porth, C. Xia, R. Keppens, Reconnection and particle acceleration in interacting flux ropes-II. 3D effects on test particles in magnetically dominated plasmas, Mon. Notice. Royal. Astron. Soc. 471 (2017) 3465–3482.
[76] M. Gordovskyy, P.K. Browning, R.F. Pinto, Combining MHD and kinetic modelling of solar flares, Solar stellar Astrophys. (2018).
[77] G. Lapenta, Self-feeding turbulent magnetic reconnection on macroscopic scales, Phys. Rev. Lett. 100 (23) (2008) 235001.
[78] E.G. Zweibel, M. Yamada, Magnetic reconnection in astrophysical and laboratory plasmas, Annu. Rev. Astron. Astr. 47 (2009) 291–332.
[79] K.D. Makwana, R. Keppens, G. Lapenta, Study of magnetic reconnection in large-scale magnetic island coalescence via spatially coupled MHD and PIC simulations, Phys. Plasmas. 25 (8) (2018) 082904.
[80] B.J. Zhu, H. Yan, D.A. Yuen, Y.L. Shi, Electron acceleration in interaction of magnetic islands in large temporal-spatial turbulent magnetic reconnection, Earth. Planet. Phys. 3 (1) (2019) 17–25.
[81] C.E. Parnell, T. Neukirch, J.M. Smith, E.R. Priest, Structure and collapse of three-dimensional magnetic neutral points, Geophys. Astro. Fluid. 84 (3-4) (1997) 245–271.
[82] R.N. Sudan, Generation of ultra-high magnetic fields by high power lasers, laser interaction and related plasma phenomena, Proceedings of the AIP Conference 318(1994) 91–96.
[83] J.B. Taylor, Relaxation and magnetic reconnection in plasmas, Rev. Mod. Phys. 58 (1986) 741–763.
[84] N. Gopalswamy, A. Lara, R.P. Lepping, M.L. Kaiser, D. Berdichevsky, O.C. St.Cyr, Interplanetary acceleration of coronal mass ejections, Geophys. Res. Lett. 27 (2000) 145.
[85] A.O. Benz, Flare observations, Liv. Rev. Solar Phys. 5 (1) (2008).
[86] N.S. Gopalswamy, M.L. Yashiro, R.A. Kaiser, J.L. Bougeret, Characteristics of coronal mass ejections associated with long wavelength type II radio bursts, J. Geophys. 106 (29) (2001) 219.
[87] A. Caspi, S. Krucker, R.P. Lin, Statistical properties of super-hot solar flares, Astrophys. J. 781 (1) (2014).